AI-directed voxel extraction and volume EM identify intrusions as sites of mitochondrial contact

Benjamin S. Padman,[2,5,*] Runa Lindblom,[1,3] and Michael Lazarou[1,2,3*]

[1]Walter and Eliza Hall Institute of Medical Research, Parkville, Victoria, Australia
[2]Department of Biochemistry and Molecular Biology, Biomedicine Discovery Institute, Monash University, Melbourne, Australia
[3]Department of Medical Biology, University of Melbourne, Melbourne, Victoria, Australia
[5]Present address: Telethon Kids Institute, Perth Children's Hospital, Nedlands, Western Australia, Australia

Correspondence: Benjamin S. Padman (benjamin.padman@uwa.edu.au), Michael Lazarou (lazarou.m@wehi.edu.au)

ABSTRACT

Membrane contact sites (MCS) establish organelle interactomes in cells to enable communication and exchange of materials. Volume electron microscopy (vEM) is ideally suited for MCS analyses, but semantic segmentation of large vEM datasets remains challenging. Recent adoption of artificial intelligence (AI) for segmentation has greatly enhanced our analysis capabilities. However, we show that organelle boundaries, which are important for defining MCS, are the least confident predictions made by AI. We outline a segmentation strategy termed AI-directed Voxel Extraction (AIVE), that combines AI predictions with image electron signals to confidently segment membrane boundaries irrespective of the AI model used. We demonstrate the precision conferred by AIVE by applying it to the quantitative analysis of organelle interactomes from multiple FIB-SEM datasets. Through AIVE, we discover a previously unknown category of mitochondrial contact that we term the mitochondrial intrusion. We hypothesise that intrusions serve as anchors that stabilize MCS and promote organelle communication.

Introduction

Organelles allow eukaryotic cells to compartmentalize cellular pathways that would normally be incompatible in a shared environment. However, compartmentalization also isolates key processes that depend on one another. To link isolated pathways, cells dynamically regulate interactions between organelles via physical points of contact called Membrane Contact Sites (MCSs) [1], that mediate inter-organelle communication, material exchange, tethering and structural support [2]. For example, cardiolipin synthesis at the inner mitochondrial membrane requires the precursor lipid phosphatidic acid, which is synthesised by the endoplasmic reticulum (ER) [3]; without adequate MCSs between mitochondria and the ER, cardiolipin synthesis would halt. MCSs are now widely accepted to be essential for cellular homeostasis [4], and MCSs have been reported between almost every conceivable combination of organelles [5-8]. Collectively, the interaction network between these various organelles is referred to as the "organelle interactome" [9].

Meaningful analysis of the organelle interactome poses a major technical challenge because MCSs represent small points of contact between comparatively large structures. Optical microscopy is suitable for imaging large interacting structures, but the separation distances of an MCS at 10 nm to 35 nm [10] are smaller than the resolvable limits of light. Biochemical methods also have limitations, since most sample preparation methods typically remove structural and spatial context from the MCS prior to analysis [11]. This is why volume electron microscopy (vEM) techniques are frequently referred to as the *"gold standard"* for studying MCS structure [10].

Volume EM (vEM) methods based on scanning electron microscopy (SEM), such as Focussed Ion Beam SEM (FIB-SEM) or Serial Block Face SEM (SBF-SEM), enable the ultrastructural visualisation of membrane structures within cellular scaled volumes. However, analysis of large vEM datasets poses a major challenge since the structures detected require semantic segmentation (hereafter segmentation) and object classification before they can be quantitatively analysed, and this process has historically relied on the manual labelling of each organelle membrane by hand to define their boundaries. This reliance on human input represents a major bottleneck in the throughput of vEM methods, and the traditional approaches to image segmentation can no longer keep pace with the rate of data acquisition [12], which increases every year [13]. Given these challenges, it can be argued that the rapid adoption of Machine Learning and Deep Learning based approaches for vEM was inevitable [14, 15]. AI-based image segmentation approaches are now widely accepted in the field of vEM, but they are not without their own potential flaws when it

comes organelle boundaries. Segmentation aims to define where an object is, but it also aims to define where an object isn't. The transition between the presence or absence of an object defines its bounding surface in a vEM dataset. The challenge arises when organelle surfaces segmented via AI-based approaches represent locations where a trained model was equally certain about the presence and absence of that object, and this can become problematic for MCS analyses.

Here, we demonstrate that the least certain model predictions made via AI-based image segmentation occur predominantly at the bounding surface of an object, which is the most important location for MCS analyses. This boundary uncertainty causes variable results between AI models, and directly impacts the reliability and accuracy of ultrastructural measurements. We outline and benchmark a strategy called AI-directed Voxel Extraction (AIVE) designed to negate this limitation. Through a series of benchmarking experiments, we demonstrate AIVE's capacity to reduce the variability between different AI models and confer greater consistency in MCS analyses in cultured cells and tissues alike. We conduct a comprehensive analysis of FIB-SEM datasets acquired from HeLa cells revealing the existence of a previously undescribed morphological category of mitochondrial MCSs that we term mitochondrial intrusions. The benefits of mitochondrial intrusions include increased surface area of membrane contacts between organelles that may serve as an anchor to enhance crosstalk efficiency.

Results

AI based approaches for the segmentation of volume EM data

AI based image segmentation uses information learned from training data to create statistical or deductive frameworks (termed a model), so that predictions can be made about new unseen data. Given the large datasets that can be generated using FIB-SEM imaging of cells, there are clear advantages in using AI based approaches to automate membrane segmentation [16]. To demonstrate, we used a test dataset of approximately 3.5 μm^3 in volume (Dimensions; X, 2.4 µm (740 px); Y, 1.2 µm (370 px); Z, 1.2 µm (121 slices)), that originates from a larger 655 μm^3 dataset that will be discussed later in greater detail (Fig.4-8). The test dataset was used to train a random forest model to identify cellular membranes detected via FIB-SEM imaging (Fig.1A-B). This trained model generated probability (P) values indicating the likelihood that a membrane is present at each voxel in the dataset (Fig.1C). To complete the segmentation of these membranes (Fig.1D-E), the scalar P values were binarized by assigning a probability threshold (Fig.1D) or an isosurface value (Fig.1E) to generate a 3D result. The decision threshold is a critical parameter in AI-based image segmentation, because it defines the boundary of each segmented object, thereby defining an object's volume, surface area and contact with other objects. When selecting a threshold value, a mid-point P value of 50% appears to be a logical choice (Fig D-E), but 50% probability values represent where the model was equally certain about the presence and absence of an object, making it the least certain prediction. Deep learning methods like convolutional neural networks (CNNs) do not use a pre-chosen decision threshold, but the output layer of a CNN learns parameters akin to a threshold in order to generate a binary result [17, 18]. Regardless of the methods used to predict and binarize results, the decision thresholds control the ultimate conclusions drawn by a model, and by extension, the boundary of each object.

When presented with the same data, different AI algorithms make different predictions about the boundaries of an object, and these differences can affect interpretations of organelle ultrastructure and membrane contacts [19]. To demonstrate this, we trained six machine learning models based on different algorithms of varying complexity to detect membranes in the same test dataset from Fig.1B. All six models were trained in the detection of membranes using the exact same training samples and feature data before application to the same test dataset (Fig.1F), and therefore any variability between results would be due to their algorithmic differences. Each model was capable of membrane detection (Fig.1F), but key differences existed between their

114 results. By visualizing the differences in predicted values (ΔV) from each model (Fig.1G; ΔV), it can
115 be demonstrated that most of the predictions agree between models, but the disagreements that
116 do occur are almost exclusively localized to the membrane boundaries (Fig.1G). This uncertainty
117 about the position of a membrane boundary would negatively impact the reliability of any
118 organelle contact analysis, since it confounds the measurement of membrane separation
119 distances.

120 AIVE: a tool for accurate automated segmentation of cellular membranes

121 To improve the accuracy of membrane boundaries obtained from AI segmentation methods, and
122 to generate greater consensus across different AI algorithms, we developed an approach termed
123 AI-directed voxel extraction (AIVE)[16, 20]. AIVE combines the automated segmentation outputs
124 of an AI model with the ground truth of the volume EM data. Applying AIVE involves two major
125 steps: 1) Segmentation of cellular membranes with an AI (as in Fig 1), and then 2) multiplication of
126 the AI membrane prediction with the original EM data to extract only those voxels belonging to a
127 membrane. The benefit of AIVE for membrane boundary detection is that the regions of uncertain
128 AI prediction are accounted for by the intensity of signals in the EM data. For example, at a
129 boundary where the AI is uncertain, if the EM voxels have little to no intensity then the AI
130 prediction of the uncertain region will not contribute to the output (Fig S1A).

131 To demonstrate the overall AIVE approach, the sample EM data and AI predictions from Fig 1 were
132 applied to the AIVE workflow. First, the AI prediction was smoothened by applying a 3D Gaussian
133 blur to reduce variability between predictions (Fig.S1C). The EM data was processed using
134 Contrast Limited Adaptive Histogram Equalisation (CLAHE) (Fig.2C) to normalise differences in
135 image contrast that can occur between different data acquisitions, and median blurred to reduce
136 signal shot noise. In the final step, the voxel values from the AI predictions and the raw EM data
137 (Fig.2B-C) were multiplied to generate the AIVE output (Fig.2D). By multiplying voxel values from
138 two independent dynamic ranges (Fig.S1A), any input voxels with a value of zero were
139 automatically excluded from the output, whereas electron signals predicted by the model to
140 represent membranes were retained for segmentation (Fig 2D and Fig S1A). Importantly, this
141 strategy is not limited to membranes, since any cellular content that generates an electron signal
142 can be isolated (Fig.S1B). Like any other segmentation technique, a threshold value is required to
143 generate 3D surfaces from the AIVE dataset (Fig.S2A-C). it is important to note that values near
144 the centre of the output dynamic range (50%; 8-bit value of 128) are not equivalent to the 50%

145 probability threshold value discussed earlier (Fig.1D). This is because AIVE results are the product
146 of multiplying two independent dynamic ranges (Fig.S1A), so the centre of both dynamic ranges is
147 in fact 25% (50% × 50% = 25%; 8-bit value of 64). The premise of AIVE is therefore akin to a signal
148 masking strategy, in which electron signals detected during EM are used for the segmentation of
149 object boundaries instead of using AI predictions alone (Fig.1G). Doing so improves the accuracy,
150 precision, and consistency of membrane segmentation, as we will demonstrate through a series of
151 benchmarking experiments.

152

153 Benchmarking AIVE

154 ***AIVE enables outputs to be compared between different AI algorithms***

155 We had observed large discrepancies between membrane boundary positions segmented by
156 different AI models in the same EM dataset (Fig.1F). To benchmark AIVE and demonstrate its
157 benefits, the same AI model predictions shown in Fig.1F were applied to the AIVE workflow
158 (Fig.2E). Upon application of AIVE, the difference in values (ΔV) between each model greatly
159 reduced (compare Fig.1F-G to Fig.2E-F). Quantitation of the ΔV per image slice also demonstrated
160 that the variability between results can be more than halved by AIVE, though we note that some
161 of this improvement was due to the initial blurring of the predictions (Fig.S1C). Next, we assessed
162 how the differences between boundaries from each model would affect 3D spatial measurements.
163 This was done by selecting 30 random points near membranes (distance probes; Fig.2H; see also
164 Video 1), then measuring the distance between each point and their nearest membrane (Fig.S2D).
165 By measuring the range (Fig.2I) and relative absolute deviation (Fig.2J) of distance values recorded
166 between models for each probe, the reliability of measurements under each condition can be
167 quantified. By both measures (Fig.2I-J), AIVE processing greatly improved the consistency of
168 measurements between models, outperforming the AI predictions alone with or without the
169 application of a Gaussian blur. Together, these analyses show that AIVE enables greater consensus
170 between AI models at regions of uncertainty (membrane boundaries), and that AIVE can be
171 applied with any AI model chosen by a user.

172 ***AIVE improves the accuracy and precision of organelle classification***

173 The accuracy of organelle membrane segmentation is fundamentally important for the analysis of
174 organelle interactions. The AIVE framework can easily integrate organelle classification prior to the

voxel extraction step. This simply requires the preparation of binary labels that map the identity of organelles. For example, if a mitochondrion of interest were present in the dataset, its identity can be defined by drawing a label around that approximate region (Fig.3A). While this process may seem identical to conventional classification, AIVE differs in that it does not use these classification labels to define the boundaries of any organelles. Instead, the class labels are used to mask regions of the AI predictions and merely identify them as belonging to a specific organelle (Fig.3B-C). The resulting data is then processed via AIVE resulting in segmentation of membranes belonging to a specific organelle, which in the sample case is a mitochondrion (Fig.3D-E).

Class labels can be assigned manually by a human or automated using AI. To demonstrate this, we assessed the classification labels generated by a human analyst and two U-Net CNNs in the detection of one mitochondrion (Fig.3F) from the test dataset in Fig.1A. Classification by a human analyst was conducted manually on two consecutive days, while the two U-nets differed in their randomization seed during training. Mitochondrial labelling was generally similar between the classification approaches (Fig.3F), but the human classifications tended to extend further than necessary beyond the perimeter of mitochondria, whereas the U-Nets occasionally appeared to miss portions of the mitochondrion (Fig.3F; arrowheads).

To benchmark the benefits of AIVE, the binary class labels from Fig 3F were used for organelle segmentation using four different approaches: (1) Traditional instance segmentation, in which binary class labels are used to define object boundaries (Fig.3G); (2) AI Extraction (AIE), where the class labels are used to mask the AI predictions without voxel extraction (Fig.3H); (3) direct Voxel Extraction (VE), which uses the class labels to mask the normalized EM data without using AI predictions (Fig.3I); and, (4) AIVE (Fig.3J).

To understand the reconstruction results, we must first address the characteristics and limitations of conventional 3D segmentation. Specifically, 3D surfaces generated using binary segmentation alone (Fig.3G) demonstrate a noteworthy artifact called “terracing” (Fig.3G; see 3D insets), which presents as artificial plateaus [21]. The terracing is caused by abrupt (binary) changes in voxel value, which affect the local shape since contours can only be represented by a limited pool of surface topologies (2^8; 256) [22], of which only 15 are unique [23]. In contrast, the additional information present within a 8-bit scalar datasets, such as those generated by AIE, VE and AIVE (Fig. 3H-J) can theoretically adopt $>1.8\times10^{19}$ (256^8) different polygon configurations at each voxel and interpolate fractional angles with spatial anisotropy relative to the voxel grid [23]. Therefore,

206 by moving from binary labels to scalar values we can generate a more natural contour from our
207 voxel grid, as shown by the surface details shown in Fig. 3H-J compared to Fig. 3G.

208 Next, we benchmarked AIVE against voxel extraction (VE) and AI extraction (AIE). VE prevents
209 terracing (Fig. 3H), but the scalar data also includes irrelevant electron signals. Similarly, AIE
210 reduces terracing (AIE; Fig.4I), but the disadvantages of relying on AI predictions alone for
211 membrane boundaries have already been outlined (Fig.1-2). To directly show how the different
212 approaches influence the reliability of contact site analyses, we quantified the variability of
213 distance measurements between classification labels for each of the scalar 3D datasets (Fig.3H-J).
214 We conducted 3D measurements (Fig.3K) using a new set of 3D distance probes nearer to a
215 mitochondrion (Fig.S1D; see also Video 2), since the original 3D probe locations had no relation to
216 a specific organelle (Fig.2H). As demonstrated by the range (Fig.3L) and relative absolute deviation
217 (Fig.3M) of distance values recorded by each 3D probe, the distance measurements recorded for
218 AIVE datasets were very consistent between each of the differing class labels as opposed to VE
219 and AIE (Fig.3F). Therefore, AIVE substantially improves the precision and consistency of 3D spatial
220 measurements in volume EM datasets.

221 We next conducted a benchmarking experiment to compare the accuracy of measurements
222 generated via AIVE to a known standard point of reference. Nuclear Pore Complexes (NPCs) are
223 large protein channels in the nuclear envelope which mediate cargo transport between the
224 interior and exterior of the nucleus. NPC structure is highly conserved among eukaryotes, which is
225 why they are often used as a reference standard for benchmarking microscopy methods [24]. The
226 test dataset used in figures 1-3 originated from a larger cellular volume that also contained a
227 portion of nuclear envelope (Fig.4B). Using the manual classification strategy described in Fig. 3A-J,
228 we processed a portion of the nuclear envelope containing 18 individual nuclear pores (Fig.S1E),
229 via VE (Fig.3N), AIE (Fig.3O), or AIVE (Fig.3P). The same 18 pores were isolated from each
230 processed dataset and aligned using the exact same transforms (see methods for further detail;
231 Fig.S1F) to compare each processing method (Fig.3Q-T) against recent NPC structures [25, 26].
232 Data processed by VE alone (Fig.3N) rarely yielded a detectable pore because they were often
233 occluded by irrelevant electron signals (Fig.3Q). In contrast, central transport channels were
234 consistently detected in the data processed AIE alone (Fig.3O) or AIVE (Fig.3P), but the average
235 diameter of those pores differed between processing methods (Fig.3Q); 42.9 nm for AIE alone
236 compared to 52.4 nm for AIVE. We related these pore measurements to reported values from two

237 independent studies from 2021 (arrowheads in Fig.3Q), which used cryo-electron tomography to
238 resolve NPC structures *in cellulo* [25, 26]. Schuller *et al.* reported that human NPCs have a central
239 channel diameter of 57 nm (Fig.3Q; black arrowhead) [25]. The AIE processed data differs from
240 this value by 14.1 nm, whereas the AIVE results differed by only 4.6 nm. The study by Zimmerli *et*
241 *al.* was not conducted in human cells [26], but we include their findings because they provide
242 valuable context for the distribution of our measurements (Fig.3Q; value range indicated by white
243 arrowheads). Unlike data processed using VE or AIE alone, the majority of the AIVE processed
244 nuclear pores had a diameter within the published reported range. Renderings of the median
245 averaged pores from each processing method are also provided (Fig.3R-T; shown in purple), for
246 visual comparison with the human NPC structure published by Schuller *et al.* (Fig.3R-T; shown in
247 orange [25]). Collectively, our benchmark experiments show that AIVE processing substantially
248 improves both the precision and accuracy of spatial measurements in volume EM datasets.

249

250 Mapping organelle interactomes using AIVE

251 *Compositional analysis of cellular membranes via AIVE*

252 Having outlined the technical basis and advantages of AIVE, we next demonstrated some of the
253 biological insights AIVE can yield when applied to large volume datasets. We aimed to characterise
254 mitochondrial interactions with other cellular organelles in three FIB-SEM datasets from HeLa cells
255 that were processed using AIVE (Set #1, Fig.4B; Set #2, Fig.4C; Set #3, Fig.4D; see Video 3). As
256 mentioned previously, the test dataset used in our benchmarking experiments (Fig.1-3) originated
257 from a small region (Fig.4A) within one of these datasets. AIVE data can be subjected to a wide
258 range of analyses (Fig.4-8), the simplest being direct quantification of membrane volume (Fig.4F-
259 H). Set #1 (654.0 μm^3 total volume of dataset) contained the highest proportion of organellar
260 membranes (84.7 μm^3; 12.9% of total volume). Due to the prominence of the cellular nucleus in
261 sets #2 & #3, organellar membranes represented a substantially lower proportion of their total
262 volume (Set #2, 858.8 μm^3 total, 59.4 μm^3 organellar membrane; Set #3, 640.9 μm^3 total, 39.1 μm^3
263 organellar membrane). The nucleus in Set #2 is noteworthy (Fig.4C), as it also contained multiple
264 examples of nucleoplasmic reticulum tubes spanning the interior of the nucleus [27]. Excluding the
265 nuclear envelope from subsequent analyses reveals striking similarities in the distribution of
266 membrane between organelles across the datasets (Fig.4E-G), with the ER being the most
267 abundant category of organellar membrane, followed closely by mitochondrial membranes.

268 Intracellular vesicles and Golgi apparatus were the next most abundant categories of organellar
269 membrane, but Golgi apparatus was not detected Set #2 (Fig.4F); coincidentally, Set #2 also
270 contained a lower proportion of early and late endosomal membranes than in the other two
271 datasets. To explore these datasets in greater detail, we next turned our attention to individual
272 mitochondria.

273 ***Quantitative analysis of mitochondrial morphology via AIVE.***

274 The three datasets (Fig.4B-D) collectively contained 186 individual mitochondria. Morphometric
275 analysis of these mitochondria based on their membranes alone would have limited value, since it
276 wouldn't include the mitochondrial interiors or bulk morphology, which is why our machine
277 learning models were also trained to classify materials other than membrane. For example, the
278 prediction results for "Matter" (Class 3), are specifically designed to represent any electron dense
279 non-membranous materials such as the mitochondrial matrix (Fig.S1B). This additional class
280 allowed us to "fill" the mitochondria by multiplying the matter class with the mitochondrial class
281 labels, then adding the result to the AIVE membrane outputs for the corresponding mitochondria.
282 In addition, the filling process enables imputation of the matrix of each mitochondrion.

283 Morphometric analyses, including measurements of mitochondrial volume, membrane surface
284 area, volume of matrix, shape, and length were applied to all 186 mitochondria. Based on the
285 morphometric analyses, six outlier mitochondrial morphologies were identified (Fig.5A-F). This
286 included the smallest mitochondrion, whose total volume was only 0.035 μm^3 (Fig.5A). As a point
287 of comparison, the smallest mitochondrion was approximately one-hundredth the volume of the
288 largest mitochondrion (Compare Fig.5A with Fig.5B), demonstrating a wide range of mitochondrial
289 size. Unsurprisingly, the largest mitochondrion also possessed the greatest membrane surface
290 area (25.079 μm^2), largest volume of membrane (1.863 μm^3), and largest volume of matrix (1.605
291 μm^3) of any detected mitochondrion (Video 4). Our analyses of mitochondrial morphologies also
292 included two different metrics of mitochondrial "length" (see Video 7), in which the most
293 elongated and longest mitochondria were identified. The most elongated mitochondrion (Fig.5D;
294 11.89 aspect ratio, 9.36 µm longest-optimal path) was identified by measuring mitochondrial
295 ellipsoid aspect ratios (major axis/minor axis; Fig.5J), whereas the longest mitochondrion (Fig.5E;
296 2.91 aspect ratio; 11.229 µm long) was determined by skeletonizing the bulk mitochondrial
297 structure, then measuring the longest-optimal path through the skeleton (Fig.5K). Mitochondrial
298 sphericity was also quantified (Fig.5L; Video 5, left), leading to the identification of the most

299 spherical mitochondrion (Fig.5F; sphericity = 0.860). The wealth of morphological data that was
300 obtained also allowed us to identify the most average mitochondrion (Fig.5G, and Video 5, right),
301 that had morphological measurements closest to the average value across every metric quantified.
302 Interestingly, we also noted that mitochondrial membrane volume correlated closely (R > 0.99)
303 with matrix volume in all datasets (Fig.5I), demonstrating that internal mitochondrial architecture
304 is tightly controlled despite large variations in morphology.

305 The morphometric analyses also led to the identification of mitochondrial nanotunnels based on
306 the separation of mitochondrial matrix volumes within a mitochondrion (Fig.5C; Video 5, center).
307 The presence of mitochondrial nanotunnels in HeLa cells was unexpected since nanotunnels are
308 typically observed in cellular/tissue environments in which mitochondrial movement is physically
309 constrained [28]. To show an example of nanotunnels in a physically constrained tissue, and
310 demonstrate AIVE's utility in tissue samples, we conducted FIB-SEM and AIVE of murine skeletal
311 muscle tissue (Fig.S3). Numerous examples of mitochondrial nanotunnels were observed (Fig.S3A-
312 C; Video 6), in which mitochondria remained interconnected over distance by reaching around
313 myofibrils via nanotunnels (Fig.S3, Video 6). In addition, we observed extensive sarcoplasmic
314 reticulum networks that contacted mitochondrial nanotunnels at sites around myofibrils.
315 Collectively, these analyses show the extensive mitochondrial morphology analyses that can be
316 conducted using AIVE, across cultured cells and tissue.

317

318 ***Quantitative analysis of the mitochondrial organelle interactome via AIVE.***
319 Next, we aimed to investigate the interactions between mitochondria and other organelles,
320 including MCS, by quantifying the separation distances of each mitochondrion from the ER, early
321 endosomes (EE), late endosomes (LE), lipid droplets (LDs) and general cytosolic vesicles (VE) (Fig.6).
322 By individually indexing each mitochondrion, we were also able to quantify the separation
323 between each mitochondrion and the remainder of the mitochondrial network.

324 First, we determined the closest approach made between organelles by measuring the minimum
325 separation distance for each mitochondrion relative to each category of organelle (Fig.6A-F).
326 Closest approach values for the EE, LE, and LD organelle categories varied greatly between
327 mitochondria (Fig.6C-E), which were often several microns away from these categories of
328 organelle (Fig.6C-E). Next, the number of mitochondria in contact with each category of organelle

329 was determined by applying the standard criteria often described for membrane contact sites of <
330 35 nm separation [10]. On average, we found that 12.13% of mitochondria were in contact with an
331 early endosome, 24.96% were in contact with a late endosome, and 10.24% were in contact with a
332 LD (Fig.6G). In contrast, every mitochondrion was found to be in contact with the ER (Fig.6G), and
333 the mitochondria-ER closest approach distances never exceeded 5nm (Fig.6B). These results are in
334 close agreement with the findings of Friedman et al., [29] who reported that all cellular
335 mitochondria maintain continuous contact with the ER. Additional categories of mitochondrial
336 membrane contact were also observed, and they included interactions with other mitochondria
337 and cytosolic vesicles (Fig.6G). These results demonstrate the utility of AIVE in measuring organelle
338 interactomes, while also revealing the extent of organelle contacts, and how they vary across
339 different organelles.

340

341 ***Mitochondrial intrusions are morphological platforms for organelle interaction.***
342 Using distance-based criteria to define MCS is a valuable tool. However, we also wanted to
343 account for the magnitude of the contact area relative to the size of an organelle because it gives
344 context to the breadth of a membrane contact site. For example, small point-like interactions with
345 randomly distributed vesicles (Fig.6G), cannot be distinguished from a membrane contact that
346 covers a substantially greater surface area. We therefore sought to refine our quantitative
347 analyses of MCS by accounting for the size of interaction sites between mitochondria with the ER,
348 vesicles (VE), and other mitochondria (Fig.6H-M). By grouping distance measurements into 5nm
349 brackets ranging between 0 to 250 nm, the percentage of a mitochondrion's surface from each
350 separation distance was determined (Fig.6K-M). The analysis revealed a prominent peak in the 0
351 to 5 nm distance bracket for mitochondrial (Fig.6K) and ER distance measurements (Fig.6L;
352 Arrowheads), but not for cytosolic vesicles (Fig.6M), that were typically further away from
353 mitochondria and occupied little of the mitochondrial surface.

354 The value peak detected in the 0-5nm range caught our attention because it is a large surface of
355 contact that cannot occur between round convex spheroids (Fig.S4A & C), unless one of those
356 objects partially envelopes the other (Fig.S4B & D). Indeed, our analysis of the 0-5nm membrane
357 contacts revealed striking mitochondrial morphologies that enabled membrane contact via
358 organelle intrusion (Fig.7). The intrusions were characterised by an invagination of the outer
359 mitochondrial membrane to form a narrow cavity that protruded into the interior of a

360 mitochondrion (Fig.7; see Videos 8-9). Mitochondrial intrusions frequently contained ER
361 membranes (Fig.7A-C; Video 8), that typically occupied the entire intrusion cavity. Interestingly,
362 the ER membranes often displayed higher levels of osmium staining (EM data; Fig.7A-C), indicating
363 that the membranes are protein rich or have a unique lipid profile. Mitochondrion-to-
364 mitochondrion intrusions were also observed, in which the exterior membranes of one
365 mitochondrion intruded into an adjacent mitochondrion (Fig.7D-E; Video 9). Unlike the ER-to-
366 mitochondrion intrusions, membranes in this category of intrusion did not display increased
367 osmium staining (Fig.7D-E). We also identified a mitochondrion that was intruding into another
368 mitochondrion while simultaneously receiving an intrusion from the ER (Fig.7D; Fig.8A, See box
369 indicating Set #1, mitochondria 61 & 89). This demonstrates that mitochondria can simultaneously
370 give and receive intrusions, potentially enabling inter-organelle communication. Mitochondrial
371 intrusions lacking an intruding membrane within the cavity were also observed (Fig.7F), indicating
372 that intrusion cavities may form independently from an intruding membrane.

373 We asked why mitochondrial intrusions have not previously been reported using established EM
374 approaches. Additional morphological analyses revealed key features that can provide an
375 explanation why intrusions have not been observed until now. Of the 186 mitochondria surveyed,
376 we detected a total of 50 mitochondrial intrusions among 36 individual mitochondria (Fig.8A),
377 equating to 0.269 intrusions per mitochondrion on average. No mitochondrial morphological traits
378 appeared to correlate with the presence of an intrusion (Fig.8B), implying that the formation of a
379 mitochondrial intrusion is stochastic. Indeed, the average number of intrusions per mitochondrion
380 (0.269) was used to model a Poisson distribution that closely approximates the observed values
381 (Fig.8C). Compared to the mitochondrion, the internal volume of the average intrusion cavity was
382 miniscule (Fig.8D), and the largest sphere capable of fitting within these cavities would have a
383 radius no larger than 50.6 nm (Fig.8E), yet they often extended several hundred nanometers
384 inward (Fig.8F).

385 A mitochondrial intrusion can only be confidently identified when viewed in its entirety. This is
386 because without evidence of the entrance, an intrusion would be indistinguishable from a
387 membrane inclusion (see Fig.7D), and without evidence of the deeper intrusion, the cavity
388 entrance would appear to be a slight membrane indentation (see Fig.7A). We sought to
389 demonstrate this by calculating the probability of detecting a fully intact mitochondrial intrusion
390 via TEM imaging by using Buffon's needle problem [30]. Buffon's needle problem is a geometrical

probability and is formulated as follows: If a needle of known length (L) is randomly dropped onto an array of regularly spaced lines separated by a known distance (d), what is the probability that the needle will overlap a line after landing (Fig.S4E). In the present context, the “needles” represent mitochondrial intrusions with an average length (L) of 367.5 nm (Fig.8F), the space between lines represent TEM sections of known thickness (d), and the needles that overlap a line represent incomplete intrusions that extended into adjacent sections. The probability of detecting a fully intact intrusion can therefore be considered the inverse of Buffon’s needle problem (Fig.8G; Fig.S4E). For a hypothetical 100nm TEM section (d = 100 nm) containing a mitochondrial intrusion, there is less than a 1 in 10 chance (P = 0.087) that the intrusion will remain fully intact within that section (solid line in Fig.8G). Under these conditions, an observer would be twice as likely to observe only half of the intrusion (P = 0.177964; see dashed line, Fig.8G), which would be indistinguishable from a membrane inclusion or indentation of the outer membrane. Even if the section thickness was equal to the length of an intrusion (L = d), the probability of the structure being intact remains low (P = 0.363; solid line in Fig.8G). It is important to note that the real probability of observing an intrusion is likely even lower, since they were only present in a fraction of the mitochondria (Fig.8C). In contrast, there would be a 95% chance (P = 0.953) of an intrusion remaining intact if the Z-depth of the sampled volume spanned 5 µm (d = 5000 nm), which would not be possible using TEM, but easily achieved via FIB-SEM. These calculations demonstrate why mitochondrial intrusions have not previously been identified using historical TEM.

Taken together, by using AIVE we were enabled to discover that HeLa cell mitochondria can contact the ER (and other mitochondria) via intrusion sites (Fig.7 & 8), which provide a larger interface for surface interactions not possible between round objects (Fig.7; Fig.S4). We have also shown that these intrusion sites are more likely to be indistinguishable from a mitochondrial membrane inclusion when viewed by TEM (Fig.8G).

Discussion

In this study, we have outlined and benchmarked a technique termed AIVE for volumetric EM. AIVE enables electron signals detected via FIB-SEM to be processed for rapid 3D reconstruction and analysis with high fidelity. AIVE's fidelity is achieved by using the ground truth of EM data in the final output. In AI research, ground truth is used to describe the preferred result from a

421 trained model [31], but the original definitions of ground truth specify that it originates from
422 objective empirical measurements [32]. In the context of this manuscript, the back-scattered
423 electron signals acquired via FIB-SEM imaging represented the most objective and empirical
424 measurements that could be used for ground truth. AIVE therefore uses an objective definition of
425 ground truth by linking AI predictions to real empirical measurements. Since its inception, AIVE has
426 been applied to volumetric EM analyses of cultured cells [16, 20] and animal tissues alike (Fig.S6).
427 However, in the absence of benchmarking, it was unclear why a cell biologist might choose to
428 apply AIVE versus AI predictions alone. Here, we demonstrate that membrane boundaries are the
429 least certain areas of AI predictions. Through extensive benchmarking, we make a case for the
430 benefits of AIVE to define membrane boundaries with high fidelity that provides benefits for the
431 study of organelle ultrastructure and MCSs.

432 Mitochondrial membrane ultrastructure is tightly linked to the biochemical functions of a
433 mitochondrion [33]. For example, mitochondrial damage and dysfunction are linked to a range of
434 abnormal mitochondrial morphologies including cristae disturbances and network fragmentation
435 [34-36]. In mitochondrial diseases, abnormal morphologies can manifest as osmiophilic inclusions
436 of concentric membranes and "onion-shaped" cristae within the mitochondria [34, 35], while in
437 other cases cristae structures are diminished [37]. Mitochondrial ultrastructure can also change in
438 response to the metabolic activity of mitochondria [38], in which mitochondria undertaking
439 oxidative reactions retain defined cristae whereas those enriched in reductive reactions lack
440 cristae. The intimate association between mitochondrial structure and function lends itself to
441 exploration using volumetric EM. AIVE can therefore be used in various contexts, ranging from
442 understanding mitochondrial ultrastructure in different tissues and disease states, to
443 understanding the relationship between mitochondrial morphology and physiological and
444 biochemical status. Cristae are intricate structures of the mitochondrial inner membrane that
445 come in all manner of unusual shapes and sizes depending on cell type and metabolic status [37].
446 For example, cristae in astrocytes appear to take the shape of triangles, whereas cristae in adrenal
447 cortex cells are highly circular [33]. Cristae analyses such as these have typically been conducted
448 using 2D TEM. By applying volume EM and AIVE, we anticipate that additional fascinating features
449 of cristae structure and biology will be revealed.

450 Mitochondrial structures can dynamically adapt according to their cytosolic environment. For
451 example, mitochondria in muscle tissue form nanotunnels that enable connectivity of the

452 mitochondrial network around the physical obstruction of myofibrils [28, 39](Fig. S6). Nanotunnel
453 connectivity can increase in murine cardiac myocytes with defective calcium release from the
454 sarcoplasmic reticulum [40], indicating an adaptive role for nanotunnels. Through AIVE, we were
455 able to expand on previous studies of nanotunnels and show the extensive ultrastructure of
456 mitochondrial nanotunnel networks in murine skeletal muscle (Fig. S6B). We also revealed
457 extensive MCSs between nanotunnels and the sarcoplasmic reticulum (Figure S6C), that may play
458 a role in calcium buffering during contraction [40]. Our findings demonstrate the benefits of
459 collecting large EM volumes combined with AIVE in identifying long distance organelle connections,
460 including mitochondria via nanotunnels, and the nucleus via nucleoplasmic tubes (Fig 4C).

461 Another area of cellular biology illuminated by AIVE and volume EM was the visualization and
462 quantitation of MCSs. Through AIVE, we were enabled to undertake high resolution analyses of
463 organelle interactomes via MCSs (Figs. 5-7). The value of AIVE for MCS analyses was best
464 demonstrated by the discovery of a hitherto unknown form of mitochondrial contact that we term
465 the mitochondrial intrusion (Fig. 7). Through intrusions, mitochondria were observed to contact
466 other mitochondria or the ER. Intrusion relays in which a mitochondrion simultaneously contacted
467 the ER and other mitochondria were also observed. These interactions go beyond the binary MCSs
468 that are typically described and highlights the complexity of organelle contacts that can be
469 revealed by volume EM and AIVE. Indeed, in a previous application of AIVE with volume EM,
470 wholesale organelle-ome changes were observed in response to perturbation of a single organelle
471 family [20]. We note that mitochondrial intrusions form basally, and they are distinct from
472 previously reported mitochondrial cavities [41]. Mitochondrial cavities, induced by fragmenting
473 mitochondria through depolarization, differ greatly from intrusions in size and morphology, and in
474 contact characteristics including the lack of intramitochondrial contacts [41].

475 What might be the benefits of mitochondrial intrusions as a form of MCS? One answer is increased
476 surface area for interaction. The exterior of a mitochondrion is typically round and convex [42, 43],
477 but this is the least efficient geometry for mediating surface-to-surface interactions [44] (Fig.S3A).
478 Mitochondrial intrusions can maximize the surface area of an MCS (Fig.S3B), and therefore
479 promote the efficiency of inter-organelle communication [45]. Another potentially important
480 benefit of intrusions is that the increased contact area can serve as an anchor to stabilise an
481 otherwise fleeting MCS. Once formed, the very close proximity of membranes within intrusions (0-
482 5nm) can feasibly support tethers that support lipid transfer including the mitochondrial proteins

483 PTPIP51 and MIGA2 [46-48], that could be facilitated by Mfn1/2 for intramitochondrial intrusions,
484 and Mfn2 and VAPB for ER-mitochondria intrusions [49-51]. In contrast, MCSs involving IP3Rs
485 (inositol 1,4,5-triphosphate receptors) that facilitate calcium transfer between ER and
486 mitochondria might be too bulky for the very close contacts made by intrusions [1, 52].

487

488 Overall, we demonstrate the utility of AIVE combined with volumetric EM for understanding the
489 ultrastructure and interactome of cellular organelles, while also demonstrating its capacity to
490 reveal fascinating and unexpected features of cell biology, including the identification of
491 mitochondrial intrusions as a form of MCS.

492

493

494 **Acknowledgements:**

495 We acknowledge Gediminas Gervinskas and the Ramaciotti Centre for Cryo-Electron Microscopy,
496 Monash University for technical support with electron microscopy. And we thank Matthew Eramo
497 and Mike Ryan for the mouse tissue FIB-SEM dataset, and acknowledge Monash Animal Research
498 Platform, Monash University.

499

500 **Methods**

501 **Cell culture**

502 HeLa cells were cultured Dulbecco's modified eagle medium (DMEM) supplemented with 10 %
503 (v/v) FBS (Cell Sera Australia), 1 % Penicillin-Streptomycin, 25 mM HEPES, 1x GlutaMAX (Life
504 Technologies) and 1x non-essential amino acids (Life Technologies). Samples were prepared by
505 culturing HeLa cell monolayers on a polymer film substrate (Aclar film; 203.2 µm thick; ProSciTech),
506 which was heat-welded to the plastic surface of a 10 cm tissue culture dish with a soldering iron.
507 Three dishes were prepared, and UV sterilized before seeding approximately 6 x 10^6 HeLa cells
508 onto the Aclar film in each dish. The cells were allowed to attach under normal culture conditions
509 for 48 hrs, with replacement of the culture medium 1 hr prior to fixation.

510 **Sample preparation of HeLa cells for FIB-SEM**

511 The samples were chemically fixed with 4 % paraformaldehyde in 0.1 M phosphate buffer (pH 7.2)
512 at 37 °C for 1 hour, with overnight postfixation with 2.5 % glutaraldehyde in 0.1 M sodium
513 cacodylate buffer at 4 °C. Each polymer film was detached from their tissue culture dish before
514 being transferred to a polypropylene tray (lid of a pipette tip box) where they were immobilized by
515 heat-welding with a soldering iron. A BioWave Pro microwave system (Pelco) was used for
516 microwave assisted sample processing in all subsequent stages. Osmication was conducted using a
517 modified OTO method [53] with three microwave duty-cycles (120 s on, 120 s off) at 100 W under
518 vacuum where indicated in the following stages; 2 % (w/v) OsO_4, 1.5 % (w/v) $K_3Fe(CN)_6$ in 0.1 M
519 cacodylate buffer (pH 7.4) at 4° for 2 hours, followed by microwave processing; three MilliQ water
520 rinses; 1 % (w/v) Thiocarbohydrazide in water with microwave processing; three MilliQ water
521 rinses; then, 2 % OsO_4 in water with microwave processing. After further MilliQ water rinses, the
522 samples were *en bloc* stained with 2 % (w/v) aqueous uranyl acetate [54], followed by Walton's
523 Lead Aspartate [55], with each stain requiring three microwave duty-cycles (120 s on, 120 s off) at
524 100 W under vacuum. Microwave assisted dehydration (150 W for 40 s per stage) was performed
525 by graduated ethanol series (80 %, 90 %, 95 %, 100 %, 100 % (w/v)) followed by propylene oxide
526 (100 %, 100 % (w/v)). The samples were infiltrated with a modified Araldite 502/Embed 812 resin
527 of the following composition (described for 10 ml resin); 2.20 g Araldite 502, 3.10 g Embed 812,
528 3.05 g NMA (nadic methyl anhydride), 3.05g DDSA (dodecenylsuccinic anhydride), and 400 µL
529 BDMA (benzyldimethylamine). Infiltration was conducted using a graduated concentration series
530 in propylene oxide (25 %, 50 %, 75 %, 100 %, 100 % (v/v); 180 s at 250 W under vacuum). Final
531 embedding was conducted with minimal resin, which was polymerized at 60 °C for 48 hrs.

532 The Aclar film was peeled from each of the resin embedded cell monolayers, before using a
533 hammer to sub-divide the resin into a random assortment of shards that were pooled into a single
534 collection. Sample shards were blindly taken from the sample pool, deposited on a small droplet
535 of the Araldite 502/Embed 812 resin on the tip of a 3.2 mm diameter aluminium rod; another
536 droplet of resin was then placed on top of that shard so that another randomly selected shard
537 could be placed on top, and the process was repeated to embed sandwiches of randomly oriented
538 cells at least three monolayers thick, before final polymerization at 60 °C for 24 hr. The stacked cell
539 monolayers were hand trimmed with a razor blade before trimming with a glass knife, to expose
540 multiple monolayers for 3D FIB-SEM imaging.

541 ## Data acquisition and pre-processing

542 FIB-SEM imaging was conducted three separate times on randomly selected cells, one cell was
543 chosen from each cell monolayer. Imaging was conducted using a cryo-Helios G4 UX FIB-SEM (FEI)
544 at room temperature using the TLD detector in immersion lensing mode for back-scatter electron
545 imaging at 3.255 nm per pixel (2 kV, 100 pA, 3 µs dwell time). Ion milling was conducted at 10 nm
546 per slice (Gallium, 30 kV, 9 nA) using the Auto Slice and View (v4.1; FEI) software. All datasets were
547 spatially registered (rigid transform) using the virtual stack registration plugin in FIJI (v1.53t) [56,
548 57]. The signal normalized inputs for AIVE were generated using a pseudo-3D implementation of
549 contrast limited adaptive histogram equalisation (CLAHE), in which three different 2D CLAHE
550 calculations were made from the front (XY), top (XZ), and side (YZ) of the registered dataset. Each
551 2D calculation was made using a modified version of the CLAHE plugin released by Stephan
552 Saalfeld in 2009; this modified plugin accounts for the anisotropy of voxels in the XZ and YZ
553 directions by allowing the use of rectangular sliding window during CLAHE. The modified plugin
554 ("CLAHE_Anisotropic.class") and script for batch automation
555 ("Batch_3DCLAHE_AnisotropicXYZ.ijm") are both provided on GitHub
556 (https://github.com/BenPadman/AIVE.git).

557 ## Sample preparation & AIVE of mouse muscle tissue

558 Wildtype C57BL/6J mouse was anaesthetised at 3 weeks of age prior to dissection of the tibialis
559 anterior muscle, which was immersion fixed in 4% PFA in 0.1M phosphate buffer at room
560 temperature (1 hour). Tissue was further dissected under fixative to extract 1mm cubed samples,
561 which were immersed in secondary fixative (4% PFA, 2.5% GA in 0.1M phosphate buffer) for
562 24hrs. All subsequent sample processing stages and imaging conditions were conducted as
563 described above for cultured cell samples. Two separate FIB-SEM datasets of skeletal muscle were
564 acquired. A machine learning model was trained on 3 classes of voxel designated "Cytosol",
565 "Fibrils" and "Membrane", using 120,000 samples per class (360,000 total) to train the final model
566 with a 10-fold test cross-validation result of over 97% self-accuracy. Mitochondria were manually
567 classified in MIB as described above, and all remaining membranes were designated as
568 sarcoplasmic reticulum. The final AIVE results were calculated as described above, and
569 reconstructed in 3D by marching cubes with an isovalue of 64. All animal work was approved by
570 the Monash Animal Research Platform Ethics Committee (MARP #17628), Monash University,
571 Australia, and conducted in compliance with the specified ethics regulations.

572 ## Computational hardware

573 All presented analyses were conducted on one computer equipped with consumer-grade
574 hardware, which included an Intel® Core™ i9-9900KF CPU clocked at 3.60GHz (16 cores), 64Gb of
575 RAM at 2133MHz, one 2 Tb SSD (Samsung 970 EVO Plus) for short term storage during machine
576 learning feature calculation, two 8Tb HDD's in RAID1 for long-term storage of machine learning
577 features and results, and an Nvidia GeForce RTX 3080 Ti for deep learning and 3D rendering.

578 ## Machine learning

579 Machine learning was conducted within the Waikato Environment for Knowledge Analysis (WEKA
580 v3.9)[58]. Training features were extracted from the registered image data using the 3D Trainable
581 Weka Segmentation (TWS) plugin for ImageJ [59, 60]. As proposed in the original manuscript [59],
582 we wrote a series of custom scripts for the TWS plugin to expand and automate its capabilities;
583 these scripts have been provided on GitHub (https://github.com/BenPadman/AIVE.git). The scripts
584 were designed to minimize RAM storage requirements for general machine learning, by ensuring
585 that all image features required for training and evaluation are only calculated once prior to local
586 storage on a hard disk. Instead of calculating all features for the entire stack simultaneously, the
587 scripts only inspect a portion of the stack at a time while including the minimum number of
588 flanking slices required by the radius of a 3D image filter. This enables features to be calculated for
589 image stacks of arbitrary length at the cost of wasted computation on flanking slices. Furthermore,
590 the script generates features incrementally by grouping image filter calculations into subsets,
591 temporarily storing the results on a local hard disk, then merging them to generate final feature
592 stacks for each slice (see script: "PART1_3DFeatSplitter_Sigma8.bsh"). Our approach also includes
593 the calculation of additional custom 2D features (see script: "PART2_2DFeatSplitter.bsh"), which
594 are merged with the original 3D feature stacks (see script:
595 "PART3_Combine3Dand2DFeatures.bsh") allowing us to calculate 175 features per slice. The
596 scripts required to execute this process are provided. In a departure from the TWS plugin all
597 training annotations were generated externally, by using the Microscopy Image Browser (MIB) to
598 generate label images where each training class is defined by the numerical value of a voxel (value
599 of 1 for class 1, value of 2 for class 2, etc). A script was then used to import each training label
600 image into TWS with its corresponding feature stack (Fig. 1G), to extract feature measurements
601 from a predetermined number of randomly selected voxels per class (see script:
602 "CorePartA_ExtractTrainingData_ArbitraryClassNum.bsh"). The feature data extracted via this

603 script can then be pooled using the “append” function in WEKA, then imported into WEKA Explore
604 for analysis and machine learning to generate various trained models, as was shown in Figures 1-3.
605 These trained models are loaded by a final script
606 (“CorePartB_ApplyClassifierToFeatureStacks.bsh”), which is designed to evaluate pre-existing
607 feature stacks.

608 These scripts were used for machine learning throughout the manuscript as follows. The analyses
609 in figures 1-3 used models trained to detect three classes of material; “Sol” (Class 1), representing
610 granular protein content of the cytoplasm and nucleus; “Matter” (Class 2), representing electron-
611 dense homogenous materials that do not belong to a membrane (i.e. mitochondrial matrix);
612 “Memb” (Class 3), representing genuine cellular membranes. The division of non-membranous
613 materials into two classes was aimed to account for the class imbalance problem; Training
614 annotations were drawn by hand in MIB. For the analyses shown in figures 1-2, feature stacks for
615 each of the three altered test datasets were generated separately before using a shared pool of
616 training labels to extract feature measurements for 1500 voxels per-class-per-slice from eight
617 slices (12000 samples per class, 36000 samples per stack, 108000 feature measurements total).
618 For the training of the six models in Figures 1-2; RF (Random Forest), J48 (the java compatible
619 extension of Ross Quinlan’s C4.5 classifier), MLP (Multi-Layer Perceptron), DT (Decision Table),
620 JRip (java compatible propositional rule-based RIPPER), and PART (Projective Adaptive Resonance
621 Theory neural network), algorithm specific parameters are enclosed within the training logs we
622 have provided for each model (See GitHub: https://github.com/BenPadman/AIVE.git). Differences
623 between model outputs were calculated using ImageJ, by calculating the absolute difference in
624 predicted values (ΔV) at each voxel between each model and every other model; results were
625 visualized by averaging all ΔV comparisons for a given model when compared to all others.

626 Data shown in Figures 4-8 used pooled feature data from all three datasets to train a random
627 forest classifier as described above, except that training involved five unique classes of material.
628 The first three of these classes were used to detect non-membrane materials: “Void” (Class 1),
629 representing the homogenous extracellular regions that lack an electron signal; “Sol” (Class 2),
630 representing granular protein content of the cell and nucleus; “Matter” (Class 3), representing
631 electron-dense homogenous materials that do not belong to a membrane (i.e. mitochondrial
632 matrix). The remaining two classes (4 & 5) were sub-categories of membrane: “Memb” (Class 4),
633 representing the majority of cellular membranes, and “Vesc” (Class 5) to represent vesicular

634 membranes; the membrane sub-classes needed to be merged together to generate a final AIVE
635 result, but separation into two classes allowed the classification of cellular vesicles by machine
636 learning alone.

637

638

639 Organelle classification for AIVE

640 Some of the raw classifier outputs described above were exploited to assist the classification of
641 organelles. For example, dilation of the "Void" class was used to assist classification of the plasma
642 membrane, whereas the Sol class labels in the nucleus were used to assist annotation of the
643 nuclear envelope. Manual labelling in MIB was then used to classify the Golgi apparatus, early
644 endosomes, late endosomes, lipid droplets. The mitochondria were also classified in this way, but
645 multiple sub-classes were used to ensure that adjacent un-fused mitochondria were considered
646 independently from one another, thus allowing each individual mitochondrion to be indexed for
647 independent analyses. The ER was classified through a process of elimination; it was the only
648 remaining unclassified membrane after classification of all other organelles. Final class labels were
649 exported from MIB as a label image. The label images containing all class labels were separated
650 into individual binary stacks, with each image representing one class of organelle. These binary
651 stacks were blurred with a 10nm gaussian filter. The 32-bit predictions generated for "Memb" and
652 "Vesc" (Classes 4 &5; described above) were combined, then multiplied with the binary stacks and
653 blurred with a 10nm gaussian filter, before merging the results with 3D CLAHE results calculated
654 earlier. This generates the final AIVE results for each individual organelle class.

655

656 U-Net training

657 Two U-Nets with 3D anisotropic architecture (same padding) were trained via stochastic gradient
658 descent with momentum (SGDM; 0.001 weight decay; 0.9 momentum), using 80×80×80 voxel
659 input patches (1040 x 1040 x 1600nm in XYZ), 5×5×5 filters, leaky ReLu activation layers (0.001
660 scale), and a dice pixel classification layer. Both U-Nets were structured with 16 input filters and 4
661 layers, and data augmentations (both 2D & 3D) were applied to 80% of the input patches during
662 training with a piecewise learning schedule (initial learn rate of 0.01; dropping by 80% every 5

663 epochs) for 35 epochs (512 iterations per epoch). The only difference between these two U-Nets
664 was the random seed value used during network initialization; The first U-Net used a random seed
665 of 1337, while the second used a value of 1338 (Fig.3F). To minimize segmentation discontinuities
666 between adjacent prediction tiles [61], each U-Net was applied using 5% tile overlap with four
667 different orientations of the dataset (original, X-flipped, Y-flipped, Z-flipped). The results were
668 then returned to their original orientations before averaging to create an ensemble result. Image
669 classification by a human image analyst in the same figure was conducted on two consecutive days
670 and required approximately 10 minutes to complete.

671

672 **3D Distance Probes**

673 To simulate the effect of result variation on membrane contact site measurements, all static
674 distance probes were assigned in accordance with standard criteria for designation of a contact
675 site (< 35 nm separation; [10]). Initial coordinates for the 3D distance probes were chosen by
676 running a stochastic simulation of diffusion limited aggregation in Mathematica (version 9). These
677 coordinates were annotated in a blank TIFF stack with identical dimensions to the test dataset, by
678 converting the voxel located at each indicated coordinate from black (value of 0) to white (value of
679 255). Probe coordinates further than 35nm from (or inside) a membrane were removed from the
680 collection by binarizing the membranes shown in Fig. 1C, dilating them by 35 nm, then subtracting
681 the un-dilated membranes from the result; any 3D probes outside the boundaries of this result
682 were deleted. This process was repeated until 30 unique probe locations were identified (Fig.2H).

683 Analyses of mitochondrial membranes (Fig.3G-M) required an additional set of criteria for the
684 distance probes, since the original 3D probes were generated without relevance to any specific
685 organelle (Fig.1H) and most were located further than 35 nm from a mitochondrion. 3D probe
686 coordinates for mitochondrial membranes were therefore generated by using the same 35nm
687 membrane boundary mask described for general membranes above in combination with an
688 additional mask representing the mitochondria, as follows; All mitochondrial class labels shown in
689 Fig.3F were averaged, binarized, dilated by 35 nm, then applied in a boolean AND operation with
690 the 35 nm membrane mask used to define the first probe positions (Fig.1H). The resulting mask
691 was then used to assign new random points as described above, until thirty new random points
692 were defined within 35nm of a membrane and within 35 nm of the mitochondrial class label

693 (Fig.4K). Value range for distance measurements (Fig.2I; Fig.3L) were calculated by subtracting the
694 minimum recorded distance from the maximum recorded distance for one probe. Relative
695 absolute deviations (aka. relative mean absolute difference) in measurements from each probe
696 (Fig.2J; Fig.3M) were calculated by dividing the mean absolute difference (difference between
697 each measurement and the mean value) of measurements by the arithmetic mean of all
698 measurements from that probe, then averaging the result.

699 Nuclear pore analyses

700 Nuclear pores were initially chosen by defining the approximate 3D coordinates of each pore in
701 the raw dataset. A cuboidal region surrounding each coordinate (300 nm on each axis) was then
702 extracted from the raw (Fig.S1F), VE (Fig.3N), AIE (Fig.3O), and AIVE (Fig.3P) image stacks. These
703 pores were then arranged into an identical orientation as follows; All four representations of data
704 (raw, VE, AIE, & AIVE) for each pore were averaged to create datasets for inter-pore alignment,
705 without biasing toward any particular method. Using the Fijiyama plugin (V4.0.11) for FIJI (v1.53),
706 Each averaged pore was manually aligned to the next pore in the sequence to generate a
707 preliminary alignment between all 18 pores, which was then refined via automatic block-matching,
708 also through Fijiyama [62]. Individual transform operations describing this alignment were then
709 composed into one rigid transformation per nuclear pore, allowing each pore to be aligned into
710 the same orientation across all four processing methods. Feret diameters of the pores were
711 measured binarizing the pore, then applying the built-in “analyse particles” function in FIJI (v1.53)
712 at the centrally aligned slice of the pore. All depictions of the individual nuclear pores are shown
713 post-alignment (Fig.3N-P; Fig.S1F), to account for the variable orientation of some pores in the
714 original dataset (Fig.S1E).

715

716 3D rendering and numerical analyses

717 All 3D surfaces were generated using the marching cubes algorithm with octree binning (256
718 points per leaf) in ParaView (v5.7). Distance measurements and mapping for visualization were
719 conducted in ParaView, by calculating the signed distance field for one polygonal mesh then
720 measuring the field value at each vertex of a second polygonal mesh. The signed distance fields
721 were calculated using a custom ParaView filter proposed in a blog post by Cory Quammen
722 (Technical leader in Scientific Computing Team; Kitware); the filter has been provided. All 3D

renderings were generated using the Cycles render engine in Blender (v2.93). All other morphometric analyses were conducted using the MorpholibJ plugin for FIJI [63]. Difference in voxel values (ΔV) were calculated using the built-in “image calculator” function in FIJI (v1.53). Mathematica (version 9) was used for all other statistical analyses and charts, including the Buffon’s needle simulation in Fig.8.

733 # Figure Legends:

734 **Figure 1: Variable AI predictions predominantly occur at object boundaries during**
735 **segmentation.**

736 **(A-E)** 3D test data acquired via FIB-SEM imaging, showing an **(A)** overview and **(B)** inset 2D slice
737 from dataset with **(C)** corresponding predictions generated by a random forest classifier trained to
738 detect membranes, alongside **(D)** 2D binary segmentation and **(E)** 3D surfaces based on the
739 membrane predictions. **(F)** 2D slices depicting raw membrane predictions for test dataset (from
740 Fig.1B) with values (V) shown as percentage of their total dynamic range (0 to 1), made using six
741 different machine learning algorithms (also provided as 3D renders in **Fig.S2A)**; RF (Random
742 Forest), J48, MLP (Multi-Layer Perceptron), DT (Decision Table), JRip, and PART (Projective
743 Adaptive Resonance Theory). **(G)** Visual depiction of the absolute difference in voxel values (ΔV)
744 between each prediction from F, showing the average value difference for each 2-way value
745 comparison as a percentage of the total dynamic range (0 to 1).

746

747 **Figure 2: AI-directed voxel extraction (AIVE) minimizes the influence of variable AI**
748 **predictions.**

749 **(A-D)** Flow chart depicting the technical basis of AI-directed voxel extraction (AIVE), in which **(A)**
750 raw 3D data from the FIB-SEM is used to **(B)** train and apply a classifier model to generate
751 probability maps depicting the location of cellular membranes (dynamic range, 0 to 1), while **(C)**
752 intensity values from the original dataset are normalized via CLAHE (dynamic range, 0 to 255); **(D)**
753 values from B are then multiplied by values from C (see also **Fig.S1A**), which isolates the voxel
754 values belonging to a membrane to generate raw AIVE data (application of AIVE to other classes of
755 signal provided in **Fig.S1B**). **(E)** 2D slices depicting raw AIVE data generated using each algorithm
756 shown in Fig.1F (3D renders of the same data provided in **Fig.S2C**), and **(F)** averaged ΔV values for
757 each 2-way comparison between one AIVE output and each of the other outputs (both shown as a
758 percentage of 8-bit dynamic range; 0 to 255). **(G)** Quantification of the average ΔV per slice for
759 each 2-way comparison made between the model predictions (Fig.1F-G) and between AIVE
760 outputs (E-F) generated using those same model predictions (quantitation and 3D renders of
761 blurred AI predictions shown in **Fig.S1C** & **Fig.S2B** respectively). **(H)** 3D rendering of membrane
762 surfaces from the test dataset (from Fig.1E) viewed from the front and above, indicating the

positions of the static 3D probes used to benchmark membrane distance measurements (membranes nearest to each 3D probe are indicated by red shading; see Video 1 for rotation animation depicting probe positions). **(I)** Quantification of the distance between each 3D probe (shown in H) and the nearest membranes detected by the six models shown in Fig.1F (raw distance measurements provided in **Fig.S2A**), after segmentation of the raw predictions, blurred AI predictions, or AIVE outputs, showing **(I)** the range (min-max) for values reported by each probe between models, and **(J)** the relative absolute deviation in measurements from each probe. Plot markers in I-J indicate value for individual 3D probes. Interquartile range indicated by box, median indicated by horizontal lines, minimum and maximum indicated by whiskers in G, I & J.

Figure 3: Object classification does not alter the precision or accuracy of segmentation by AIVE.

(A-E) Flow chart depicting object classification during AIVE, in which **(A)** organelle labels and **(B)** membrane predictions are multiplied to generate **(C)** a contextually masked membrane prediction, **(D)** which is then combined with the normalized EM data to generate **(E)** AIVE data belonging to a specific organelle. **(F)** 2D examples of mitochondrial classification labels provided by one human on different days, or two 3D U-Nets with different initialization seeds. **(G-J)** 3D rendered results classified using the labels shown in Fig.3F, after classification via **(G)** conventional instance segmentation, or by using the binary labels **(H)** for selective voxel extraction (VE), **(I)** AI extraction (AIE), or **(J)** AIVE. **(K-M)** Quantitative analysis of **(K)** the distance between mitochondrial membranes and each mitochondrial 3D probe (probe locations shown in **Fig.S1D**; also see Video 2 for rotation animation depicting probe positions), **(L)** the range of values recorded by each 3D probe, and **(M)** the relative absolute deviation in 3D probe measurements, for all datasets shown in Fig.3H-J. **(N-P)** 2D maximum intensity projections of 18 individual nuclear pores, which were spatially aligned prior processing and segmentation via **(N)** VE, **(O)** AIE, or **(P)** AIVE (Unprocessed pores shown and pore locations shown in **Fig.S1E & F** respectively). **(Q)** Feret's diameter measurements of the central transport channel from each nuclear pore after segmentation via VE, AI or AIVE. (black arrowhead indicates diameter reported by Schuller *et al.* [25]; hollow arrowhead range indicates diameters reported by Zimmerli *et al.* [26] indicated by). **(R-T)** 2D projections and 3D renderings showing the median averaged data generated via by **(Q)** VE, **(R)** AI, or **(S)** AIVE (purple), with spatial alignment to the nuclear pore complex structure (orange) published in 2021

794 by Schuller *et al.* [25]. Plot markers in **K-L** indicate values for individual 3D probes. Plot markers in
795 **T** indicate measurement for individual nuclear pores. Interquartile range indicated by box, median
796 indicated by horizontal lines, minimum and maximum indicated by whiskers. Scalebars; **N-S**,
797 100nm.

798

799 **Figure 4: The compositional analysis of membranes in bulk cellular volumes via**
800 **AIVE.**

801 **(A-D)** 3D renderings of the three FIB-SEM datasets processed via AIVE for quantitative analysis,
802 showing **(A)** the test data used in Fig.1-3 alongside overviews of **(B)** the dataset it originated from
803 (Set #1; leading lines indicate location), and **(C-D)** two additional datasets processed via AIVE (Set
804 #2 & Set #3 respectively). All three overviews are shown at the same scale (See Video 3 for
805 animated cutaways of the data). **(F-H)** Compositional analysis of membrane volumes belonging to
806 non-nuclear cytoplasmic organelles in **(F)** Set #1, **(G)** Set #2, and **(G)** Set #3. See Video 3 for
807 animated cutaways of overview data. Scalebars; A, bounding box is 2400nm wide; B-D, markers on
808 scale grid for overviews are 1000nm apart.

809

810 **Figure 5: The morphometric analysis of individual mitochondria via AIVE.**

811 **(A-G)** Mitochondria of interest that were detected in the AIVE-processed datasets shown in Fig.4,
812 showing the membranes of each mitochondrion (Red) alongside its matrix (Blue), and the binary
813 skeleton calculated for its bulk morphology (Black; longest-optimal path endings shown in yellow);
814 these include **(A)** the smallest mitochondrion, **(B)** the largest mitochondrion, **(C)** a nanotunnelling
815 mitochondrion, **(D)** the most elongated mitochondrion, **(E)** the mitochondrion with the longest
816 continuous tubule, **(F)** the most spherical mitochondrion, and **(G)** the mitochondrion closest to the
817 average values detected by all morphological metrics. For animations of these data, see Video 4
818 (for **A & B**), Video 5 (for **C, F & G**), and Video 7 (for **D & E**). **(H-L)** Quantitative analysis of key
819 morphological metrics all mitochondria in each set; **(H)** box whisker chart for the total volume of
820 each mitochondrion, **(I)** a scatter chart of showing the relationship between the volume
821 membrane (x-axis) and volume of matrix (y-axis) in each mitochondrion, with **(J-L)** box whisker
822 charts showing additional metrics for **(J)** mitochondrial sphericity, **(K)** mitochondrial length, and **(L)**
823 mitochondrial elongation. See Video 4 Plot markers indicate value for individual mitochondria.

824 Hollow plot markers indicate mitochondria that were intersected by the dataset boundary; these
825 mitochondria were excluded from analyses sensitive to incomplete mitochondria (Fig.5 A, E, D, G,
826 J-L). Interquartile range for mitochondrial population indicated by box, median indicated by
827 horizontal lines, minimum and maximum indicated by whiskers. Scalebars; A-G, markers on scale
828 grid are 1000nm apart.

829

830 **Figure 6: AIVE for the analysis of the mitochondrial interactome.**

831 **(A-F)** Quantification of the closest approach distance separating each individual mitochondrion
832 from **(A)** the rest of the mitochondrial network, **(B)** the ER, **(C)** early endosomes, **(D)** late
833 endosomes, **(E)** lipid droplets, or **(F)** cytosolic vesicles. **(G)** Average percentage of all mitochondria
834 detected within 35nm of indicated organelle per set. **(H-J)** 3D rendering of distance-mapped
835 mitochondrial surfaces from a sub-region in Set #1. The mitochondrial surfaces are shaded with a
836 colorimetric scale indicating surface distances from **(H)** other mitochondria, **(I)** the ER, or **(J)**
837 cytosolic vesicles. **(K-M)** Surface area histograms for the mitochondria located within 100nm of
838 indicated organelle, depicting the average percentage of a mitochondrial surface located within
839 indicated distance of **(K)** other mitochondria, **(L)** the ER, or **(M)** cytosolic vesicles (Arrowheads in K
840 & L indicate the anomalous peak, explained in **Fig.S4A-D**). Plot markers in A-F indicate value for
841 individual mitochondria. Interquartile range indicated by box, median indicated by horizontal lines,
842 minimum and maximum indicated by whiskers. Data in G are mean ± S.D calculated for the
843 averages in each dataset. Histogram data in K-L are mean surface area percentages binned into
844 5nm distance brackets relative to the target organelle; mean values for each set are also shown.

845

846 **Figure 7: Mitochondrial intrusion sites facilitate membrane contact with the ER**
847 **and other mitochondria.**

848 **(A-C)** Examples of ER-to-Mitochondrion intrusion sites detected in **(A)** Set #1, **(B)** Set #2, and **(C)**
849 Set #3, displayed as partial (50nm) 2D averaged projections of raw EM and AIVE data (left panels),
850 rendered in 3D (centre panels), and with a colorimetric distance-map relative to the ER (right
851 panels). For animations of these data, see Video 8. Additional examples are provided in Fig.S5A-C.
852 **(D-E)** Examples of Mitochondrion-to-Mitochondrion intrusion sites detected in **(D)** Set #1 and **(E)**
853 Set #2, displayed as partial (50nm) 2D averaged projections of raw EM and AIVE data (left panels),

854 rendered in 3D (centre panels), and with a colorimetric distance-map relative to other
855 mitochondria (right panels). For animations of these data, see Video 9. Additional examples are
856 provided in Fig.S5D-E. **(F)** 3D rendered examples of empty intrusion sites detected in each dataset.
857 Scalebars, 200nm; bounding dimensions of each 3D dataset, 1.5 x 1.5 x 1.5 µm.

858

859 **Figure 8: Volume EM is essential for the analysis of mitochondrial intrusion sites**

860 **(A)** 3D rendered examples of mitochondria containing intrusion sites, with their interior cavities
861 colourized by the category of intrusion. **(B)** Quantitative analysis comparing the membrane
862 volume mitochondria in the presence or absence of mitochondrial intrusions. **(C)** Bar chart
863 showing percentage of the mitochondrial population by their number of intrusions, with plot
864 markers indicating expected values calculated by a Poisson distribution of same average. **(D-F)**
865 Quantitative analyses of each intrusion cavity by category, showing their **(D)** total interior volume,
866 **(E)** radius of the largest inscribed sphere they could enclose, and **(F)** the length of their major
867 ellipsoidal axis. **(G)** Statistical modelling of Buffon's needle problem, showing the probability of
868 detecting an intact mitochondrial intrusion (solid line) or only half an intrusion (dashed line) when
869 an intrusion is present, as a function of the Z-depth ("d") in a hypothetical FIB-SEM dataset or TEM
870 section. Plot markers in B indicates value for individual mitochondria, in D-F indicates value for
871 individual intrusion cavities. Interquartile range for each chart indicated by box, median indicated
872 by horizontal lines, minimum and maximum indicated by whiskers. Scalebars; markers on scale
873 grid are 1000nm apart.

874

875

876 **Figure S1: Supplementary AIVE descriptions and demonstrations.**

877 **(A)** Signal matrix depicting how the input values for a voxel contribute to the output value during
878 AIVE (red line indicates approximate location of threshold used for 3D rendering and
879 segmentation). **(B)** 3D examples of other various categories of electron signal processed via AIVE,
880 as detected in the test dataset shown in Fig.1. **(C)** Quantification of the average ΔV per slice for
881 each 2-way comparison made between the model predictions from **Fig.1F** after the application of
882 a 10nm Gaussian blur (3D renders of corresponding data also provided in **Fig.S2B**). **(D)** 3D
883 renderings indicating the position of each static 3D probe used for mitochondrial distance

884 measurements in Fig.3, viewed from the front and above (membranes nearest to each 3D probe
885 are indicated by red shading). See Video 2 for rotation animation showing probe positions. **(E)**
886 Maximum value projection of AIVE processed data for the nucleus used in Fig.3, depicting the
887 position of each nuclear pore used for analysis in Fig.3N-T. **(F)** Averaged value projections of the
888 unprocessed EM data after spatial alignment for analyses shown in **Fig.3N-T**. Interquartile range
889 for chart indicated by box, median indicated by horizontal lines, minimum and maximum indicated
890 by whiskers. Scalebars; C, 1000nm; D, 100nm.

891

892 **Figure S2: Data at different stages of AIVE processing.**

893 **(A-C)** 3D depictions of 2D data shown in figures 1 & 2, showing the 3D surfaces generated using **(A)**
894 raw predictions, **(B)** blurred predictions, or **(C)** AIVE with one of six different trained models (RF,
895 J48, MLP, DT, JRip, and PART). **(D)** Raw distance measurements between the 3D probes (shown in
896 Fig.2H) and membrane surfaces under every condition shown in **A-C**. **(E-G)** raw AIVE data from
897 mitochondrion #33 (set 1) displayed as a sum projection from **(E)** the front and **(F)** above (Also see
898 Video 5), with **(G)** a orthoslice montage of EM and AIVE data through the mitochondrial
899 nanotunnel (position shown by box in F). Scalebars; 500nm.

900

901 **Figure S3: AIVE of mouse skeletal muscle.**

902 **(A-C)** AIVE reconstruction of mouse skeletal muscle tissue revealing mitochondrial nanotunnel
903 connections. **(A)** 3D rendering depicting myofibrils (red), mitochondria (purple) and sarcoplasmic
904 reticulum (gold) within a volume measuring 8 x 8 x 6.2 µm FIB-SEM volume, with **(B)** a rendered
905 cutaway displaying the interconnectivity of mitochondria within the tissue (mitochondrial
906 nanotunnels indicated by black arrow-heads). **(C)** Representative example of one nanotunnel
907 linking the mitochondrial network around a myofibril. See Video 6 for animated depiction of data
908 in A-C. Scalebar distances as indicated in figure.

909

910 **Figure S4: Simulated intrusive contacts.**

911 **(A-B)** 3D renderings of simulated contact between two spheres (128 voxel diameter) with
912 colorimetric distance scale indicating the distance of Sphere #1 from Sphere #2, **(A)** when both

structures are simple spheres, or **(B)** when Sphere #2 intrudes into Sphere #1. **(C-D)** Surface area histograms depicting the surface area percentage of Sphere #1 that is located within the indicated distances of Sphere #2, **(C)** when both structures are simple spheres, or **(D)** when Sphere #2 intrudes into Sphere #1 (Arrowhead in D indicates the anomalous peak discovered in Fig.6). **(E)** Illustrative description of "Buffon's Needle Problem" with corresponding equations, which describe the probability of a randomly distributed needle of known length ("L") overlapping a line, if those lines are regularly spaced by a known distance ("d"). Histogram data in C-D are surface area percentages binned into 5 voxel distance brackets relative to Sphere #2. Scalebars in A-B, 10 voxels.

Figure S5: Additional examples of intrusive contact sites.

(A-C) Additional examples of ER-to-Mitochondrion intrusion sites, displayed as partial (50nm) 2D averaged projections of raw EM and AIVE data (left panels), rendered in 3D (centre panels), and with a colorimetric distance-map relative to the ER (right panels). **(D-E)** Additional examples of Mitochondrion-to-Mitochondrion intrusion sites, displayed as partial (50nm) 2D averaged projections of raw EM and AIVE data (left panels), rendered in 3D (centre panels), and with a colorimetric distance-map relative to other mitochondria (right panels). Scalebars, 200nm; bounding dimensions of each 3D dataset, 1.5 x 1.5 x 1.5 µm.

933 # Video Legends:

934 ## Video 1: General membrane distance probes

935 Animated rotation of the test volume, depicting the 3D membrane probe positions (from Fig.2H)
936 used for membrane distance measurements in Fig.2-3. General membranes are shown in diffuse
937 navy blue, while membranes nearest to a 3D probe are indicated by red shading.

938 ## Video 2: Mitochondrial membrane distance probes

939 Animated rotation of the test volume, depicting the 3D mitochondrial membrane probe positions
940 (from Fig.S1D) used for mitochondrial membrane distance measurements in Fig.4. Mitochondrial
941 membranes are shown in diffuse navy blue, while membranes nearest to a 3D probe are indicated
942 by red shading.

943 ## Video 3: Overview cutaways

944 Animated cutaways of the data presented in Fig.4B-D. The video begins with all organelles shown,
945 before cutting away the endoplasmic reticulum (ER) and nuclear envelope (Nu), followed by the
946 Golgi and vesicles (VE), and finally, the early endosomes (EE), late endosomes (LE), and lipid
947 droplets (LD). The video concludes by revealing these organelles in reverse order. Render key is
948 provided within the animation.

949 ## Video 4: Smallest and largest mitochondria

950 Animation depicting the structure of the smallest (Fig.5A) and largest (Fig.5B) volumed
951 mitochondria from figure 5. Render key is provided within the animation.

952 ## Video 5: Spherical, nanotunneling, and unremarkable mitochondria

953 Animation depicting the structure of the most spherical mitochondrion (Fig.5F), a nanotunneling
954 mitochondrion (Fig.5C), and the “least remarkable” mitochondrion (Fig.5G) from figure 5. Render
955 key is provided within the animation.

956 ## Video 6: AIVE of mouse skeletal muscle

957 Animation of rendered data shown in Fig.S5, displaying an AIVE reconstruction of FIB-SEM data
958 from mouse skeletal muscle tissue, measuring 8 x 8 x 6.2 µm. As the video begins, myofibrils (red)
959 and sarcoplasmic reticulum (gold) are cut away to reveal the mitochondrial network (purple).
960 Black arrowheads then appear to highlight the mitochondrial nanotunnels, as the camera pans

around the dataset. The video concludes by focussing on a specific mitochondrial nanotunnel which is tightly wrapped around a myofibril, thus connecting mitochondria on opposing sides of the myofibril.

Video 7: Most elongated and longest mitochondria

Animation depicting the structure of the most elongated (Fig.5D) and longest (Fig.5E) mitochondria from figure 5. Render key is provided within the animation.

Video 8: Intrusive contact by ER

Animation of the ER intrusions (Fig.7A-C) depicted in figure 7. The video begins with the full ROI centred around the intrusion sites, with colourations indicated by render key. As the intruding ER fades away, the mitochondrial surface is transitioned to the distance-map (0 to 100nm) colour scale shown in figure 7, before rotation of the camera vertically over the datasets. The video concludes by returning to the initial shading.

Video 9: Intrusive contact by mitochondria

Animation of the mitochondrial intrusions (Fig.7D-E) depicted in figure 7. The video begins with the full ROI centred around the intrusion sites, with colourations indicated by render key. As the intruding mitochondrion fades away, the mitochondrial surfaces are transitioned to the distance-map (0 to 100nm) colour scale shown in figure 7, before rotation of the camera vertically over the datasets. The video concludes by returning to the initial shading.

983 # References

984 1. Voeltz, G.K., et al., *Making the connection: How membrane contact sites have changed our view of*
985 *organelle biology.* Cell, 2024. **187**(2): p. 257-270.
986 2. Scorrano, L., et al., *Coming together to define membrane contact sites.* Nature Communications,
987 2019. **10**(1).
988 3. Flis, V.V. and G. Daum, *Lipid Transport between the Endoplasmic Reticulum and Mitochondria.* Cold
989 Spring Harbor Perspectives in Biology, 2013. **5**(6): p. a013235-a013235.
990 4. Schrader, M., et al., *The different facets of organelle interplay—an overview of organelle*
991 *interactions.* Frontiers in Cell and Developmental Biology, 2015. **3**.
992 5. Shai, N., M. Schuldiner, and E. Zalckvar, *No peroxisome is an island - Peroxisome contact sites.*
993 Biochim Biophys Acta, 2016. **1863**(5): p. 1061-9.
994 6. Coleman, R.A., *It takes a village: channeling fatty acid metabolism and triacylglycerol formation via*
995 *protein interactomes.* J Lipid Res, 2019. **60**(3): p. 490-497.
996 7. Wang, Y., et al., *Nanoparticle-Driven Controllable Mitochondrial Regulation through Lysosome-*
997 *Mitochondria Interactome.* ACS Nano, 2022. **16**(8): p. 12553-12568.
998 8. Venditti, R., M.C. Masone, and M.A. De Matteis, *ER-Golgi membrane contact sites.* Biochem Soc
999 Trans, 2020. **48**(1): p. 187-197.
1000 9. Valm, A.M., et al., *Applying systems-level spectral imaging and analysis to reveal the organelle*
1001 *interactome.* Nature, 2017. **546**(7656): p. 162-167.
1002 10. Jing, J., et al., *A molecular toolbox for interrogation of membrane contact sites.* The Journal of
1003 Physiology, 2019. **598**(9): p. 1725-1739.
1004 11. Huang, X., et al., *Current and Emerging Approaches for Studying Inter-Organelle Membrane Contact*
1005 *Sites.* Frontiers in Cell and Developmental Biology, 2020. **8**.
1006 12. Peng, L., et al., *The Advances and Challenges of Deep Learning Application in Biological Big Data*
1007 *Processing.* Current Bioinformatics, 2018. **13**(4): p. 352-359.
1008 13. Xu, C.S., et al., *Transforming FIB-SEM Systems for Large-Volume and*, in *Volume Microscopy*. 2020. p.
1009 221-243.
1010 14. Gallusser, B., et al., *Deep neural network automated segmentation of cellular structures in volume*
1011 *electron microscopy.* Journal of Cell Biology, 2023. **222**(2).
1012 15. Liu, L., et al., *DeepContact: High-throughput quantification of membrane contact sites based on*
1013 *electron microscopy imaging.* Journal of Cell Biology, 2022. **221**(9).
1014 16. Nguyen, T.N., et al., *ATG4 family proteins drive phagophore growth independently of the*
1015 *LC3/GABARAP lipidation system.* Mol Cell, 2021. **81**(9): p. 2013-2030 e9.
1016 17. Richard, M.D. and R.P. Lippmann, *Neural Network Classifiers Estimate Bayesian a posteriori*
1017 *Probabilities.* Neural Computation, 1991. **3**(4): p. 461-483.
1018 18. Rumelhart, D.E., G.E. Hinton, and R.J. Williams, *Learning representations by back-propagating*
1019 *errors.* Nature, 1986. **323**(6088): p. 533-536.
1020 19. Wang, Z., E. Wang, and Y. Zhu, *Image segmentation evaluation: a survey of methods.* Artificial
1021 Intelligence Review, 2020. **53**(8): p. 5637-5674.
1022 20. Lee, R.G., et al., *Quantitative subcellular reconstruction reveals a lipid mediated inter-organelle*
1023 *biogenesis network.* Nat Cell Biol, 2024. **26**(1): p. 57-71.
1024 21. Gibson, S.F.F., *Constrained elastic surface nets: Generating smooth surfaces from binary segmented*
1025 *data*, in *Medical Image Computing and Computer-Assisted Intervention — MICCAI'98*. 1998. p. 888-
1026 898.
1027 22. Lorensen, W.E. and H.E. Cline, *Marching cubes: A high resolution 3D surface construction algorithm.*
1028 ACM SIGGRAPH Computer Graphics, 1987. **21**(4): p. 163-169.
1029 23. Kim, S., et al., *A novel interpolation scheme for dual marching cubes on octree volume fraction data.*
1030 Computers & Graphics, 2017. **66**: p. 169-178.
1031 24. Thevathasan, J.V., et al., *Nuclear pores as versatile reference standards for quantitative*
1032 *superresolution microscopy.* Nature Methods, 2019. **16**(10): p. 1045-1053.

1033 25. Schuller, A.P., et al., *The cellular environment shapes the nuclear pore complex architecture.* Nature,
1034 2021. **598**(7882): p. 667-671.
1035 26. Zimmerli, C.E., et al., *Nuclear pores dilate and constrict in cellulo.* Science, 2021. **374**(6573).
1036 27. Drozdz, M.M., et al., *Formation of a nucleoplasmic reticulum requires de novo assembly of nascent*
1037 *phospholipids and shows preferential incorporation of nascent lamins.* Scientific Reports, 2017. **7**(1).
1038 28. Vincent, A.E., et al., *Mitochondrial Nanotunnels.* Trends Cell Biol, 2017. **27**(11): p. 787-799.
1039 29. Friedman, J.R., et al., *ER sliding dynamics and ER–mitochondrial contacts occur on acetylated*
1040 *microtubules.* Journal of Cell Biology, 2010. **190**(3): p. 363-375.
1041 30. Robertson, J.M. and A.F. Siegel, *Designing Buffon's Needle for a Given Crossing Distribution.* The
1042 American Mathematical Monthly, 2018. **93**(2): p. 116-119.
1043 31. Lebovitz, S., N. Levina, and H. Lifshitz-Assa, *Is AI Ground Truth Really True? The Dangers of Training*
1044 *and Evaluating AI Tools Based on Experts' Know-What.* MIS Quarterly, 2021. **45**(3): p. 1501-1526.
1045 32. Woodhouse, I.H., *On 'ground' truth and why we should abandon the term.* Journal of Applied
1046 Remote Sensing, 2021. **15**(04).
1047 33. Zick, M., R. Rabl, and A.S. Reichert, *Cristae formation-linking ultrastructure and function of*
1048 *mitochondria.* Biochim Biophys Acta, 2009. **1793**(1): p. 5-19.
1049 34. Linda, S., et al., *Mitochondrial Diseases and Myopathies: A Series of Muscle Biopsy Specimens with*
1050 *Ultrastructural Changes in the Mitochondria.* Ultrastructural Pathology, 2009. **16**(3): p. 263-275.
1051 35. Vincent, A.E., et al., *The Spectrum of Mitochondrial Ultrastructural Defects in Mitochondrial*
1052 *Myopathy.* Scientific Reports, 2016. **6**(1).
1053 36. Jenkins, B.C., et al., *Mitochondria in disease: changes in shapes and dynamics.* Trends Biochem Sci,
1054 2024. **49**(4): p. 346-360.
1055 37. Siegmund, S.E., et al., *Three-Dimensional Analysis of Mitochondrial Crista Ultrastructure in a Patient*
1056 *with Leigh Syndrome by In Situ Cryoelectron Tomography.* iScience, 2018. **6**: p. 83-91.
1057 38. Ryu, K.W., et al., *Cellular ATP demand creates metabolically distinct subpopulations of mitochondria.*
1058 Nature, 2024.
1059 39. Huang, X., et al., *Kissing and nanotunneling mediate intermitochondrial communication in the heart.*
1060 Proc Natl Acad Sci U S A, 2013. **110**(8): p. 2846-51.
1061 40. Lavorato, M., et al., *Increased mitochondrial nanotunneling activity, induced by calcium imbalance,*
1062 *affects intermitochondrial matrix exchanges.* Proc Natl Acad Sci U S A, 2017. **114**(5): p. E849-E858.
1063 41. Miyazono, Y., et al., *Uncoupled mitochondria quickly shorten along their long axis to form indented*
1064 *spheroids, instead of rings, in a fission-independent manner.* Scientific Reports, 2018. **8**(1).
1065 42. Giacomello, M., et al., *The cell biology of mitochondrial membrane dynamics.* Nature Reviews
1066 Molecular Cell Biology, 2020. **21**(4): p. 204-224.
1067 43. Lackner, L.L., *The Expanding and Unexpected Functions of Mitochondria Contact Sites.* Trends in Cell
1068 Biology, 2019. **29**(7): p. 580-590.
1069 44. Hertz, H., *Ueber die Berührung fester elastischer Körper.* Journal für die reine und angewandte
1070 Mathematik, 1882. **1882**(92): p. 156-171.
1071 45. Scorrano, L., et al., *Coming together to define membrane contact sites.* Nat Commun, 2019. **10**(1): p.
1072 1287.
1073 46. Yeo, H.K., et al., *Phospholipid transfer function of PTPIP51 at mitochondria-associated ER*
1074 *membranes.* EMBO Rep, 2021. **22**(6): p. e51323.
1075 47. Freyre, C.A.C., et al., *MIGA2 Links Mitochondria, the ER, and Lipid Droplets and Promotes De Novo*
1076 *Lipogenesis in Adipocytes.* Mol Cell, 2019. **76**(5): p. 811-825 e14.
1077 48. Kim, H., et al., *Structural basis for mitoguardin-2 mediated lipid transport at ER-mitochondrial*
1078 *membrane contact sites.* Nat Commun, 2022. **13**(1): p. 3702.
1079 49. Naon, D., et al., *Splice variants of mitofusin 2 shape the endoplasmic reticulum and tether it to*
1080 *mitochondria.* Science, 2023. **380**(6651): p. eadh9351.
1081 50. De Vos, K.J., et al., *VAPB interacts with the mitochondrial protein PTPIP51 to regulate calcium*
1082 *homeostasis.* Hum Mol Genet, 2012. **21**(6): p. 1299-311.
1083 51. Stoica, R., et al., *ER-mitochondria associations are regulated by the VAPB-PTPIP51 interaction and*
1084 *are disrupted by ALS/FTD-associated TDP-43.* Nat Commun, 2014. **5**: p. 3996.

1085 52. Csordas, G., et al., *Imaging interorganelle contacts and local calcium dynamics at the ER-*
1086 *mitochondrial interface.* Mol Cell, 2010. **39**(1): p. 121-32.
1087 53. Seligman, A.M., H.L. Wasserkrug, and J.S. Hanker, *A new staining method (OTO) for enhancing*
1088 *contrast of lipid--containing membranes and droplets in osmium tetroxide--fixed tissue with*
1089 *osmiophilic thiocarbohydrazide(TCH).* J Cell Biol, 1966. **30**(2): p. 424-32.
1090 54. Silva, M.T., F.C. Guerra, and M.M. Magalhaes, *The fixative action of uranyl acetate in electron*
1091 *microscopy.* Experientia, 1968. **24**(10): p. 1074.
1092 55. Walton, J., *Lead aspartate, an en bloc contrast stain particularly useful for ultrastructural*
1093 *enzymology.* J Histochem Cytochem, 1979. **27**(10): p. 1337-42.
1094 56. Arganda-Carreras, I., et al., *Consistent and Elastic Registration of Histological Sections Using Vector-*
1095 *Spline Regularization*, in *Computer Vision Approaches to Medical Image Analysis*. 2006. p. 85-95.
1096 57. Rueden, C.T., et al., *ImageJ2: ImageJ for the next generation of scientific image data.* BMC
1097 Bioinformatics, 2017. **18**(1).
1098 58. Frank, E., et al., *Data mining in bioinformatics using Weka.* Bioinformatics, 2004. **20**(15): p. 2479-
1099 2481.
1100 59. Arganda-Carreras, I., et al., *Trainable Weka Segmentation: a machine learning tool for microscopy*
1101 *pixel classification.* Bioinformatics, 2017. **33**(15): p. 2424-2426.
1102 60. Schindelin, J., et al., *Fiji: an open-source platform for biological-image analysis.* Nat Methods, 2012.
1103 **9**(7): p. 676-82.
1104 61. Huang, B., et al., *Deep Convolutional Segmentation of Remote Sensing Imagery: A Simple and*
1105 *Efficient Alternative to Stitching Output Labels*, in *IGARSS 2018 - 2018 IEEE International Geoscience*
1106 *and Remote Sensing Symposium*. 2018. p. 6899-6902.
1107 62. Fernandez, R. and C. Moisy, *Fijiyama: a registration tool for 3D multimodal time-lapse imaging.*
1108 Bioinformatics, 2021. **37**(10): p. 1482-1484.
1109 63. Legland, D., I. Arganda-Carreras, and P. Andrey, *MorphoLibJ: integrated library and plugins for*
1110 *mathematical morphology with ImageJ.* Bioinformatics, 2016. **32**(22): p. 3532-3534.

1111

Figure 1

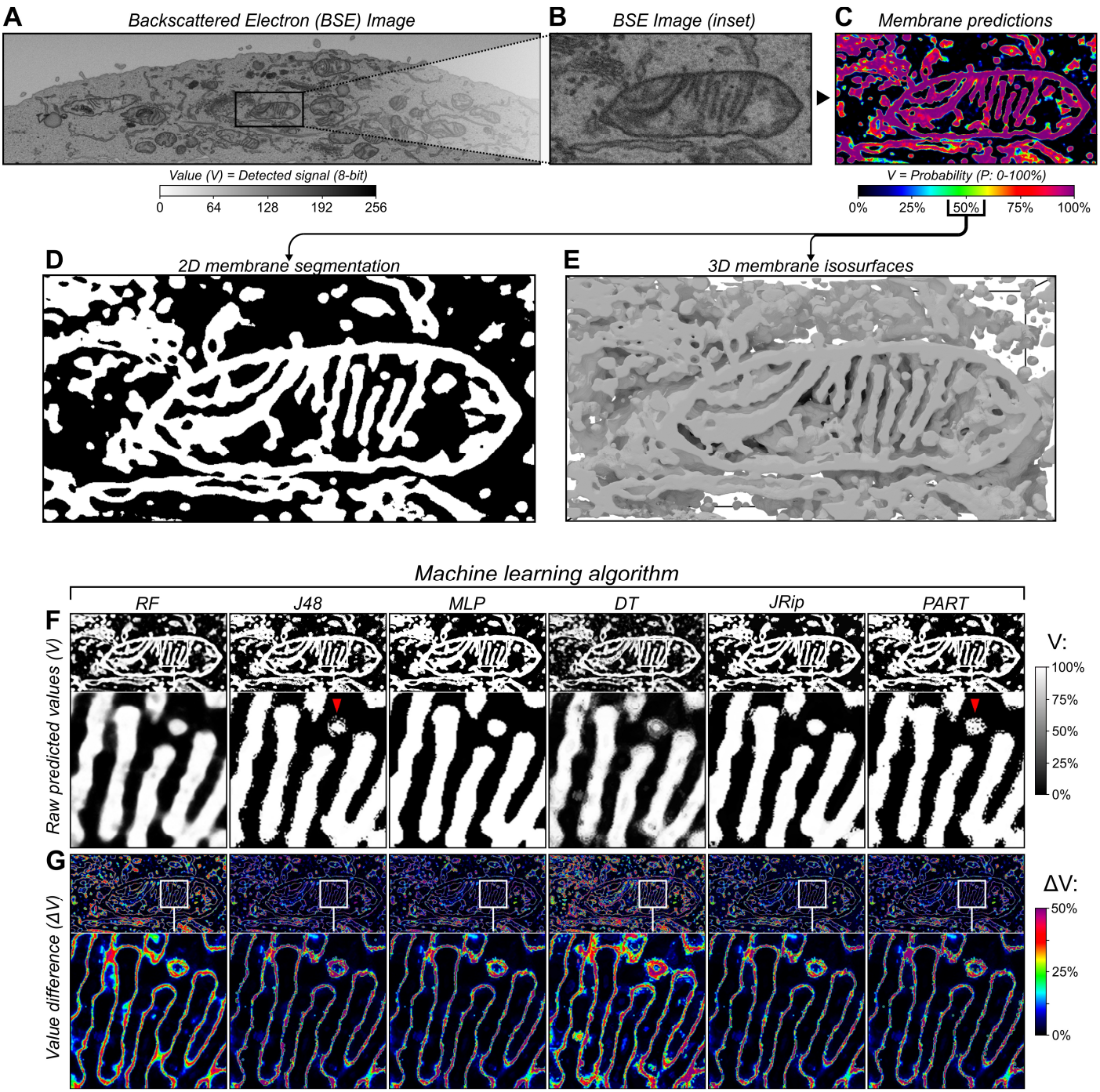
A
Backscattered Electron (BSE) Image
B
BSE Image (inset)
C
Membrane predictions
Value (V) = Detected signal (8-bit)
0
64
128
192
256
V = Probability (P: 0-100%)
0%
25%
50%
75%
100%
D
2D membrane segmentation
E
3D membrane isosurfaces
Machine learning algorithm
RF
J48
MLP
DT
JRip
PART
F
Raw predicted values (V)
V:
100%
75%
50%
25%
0%
G
Value difference (ΔV)
ΔV:
50%
25%
0%

Figure 2

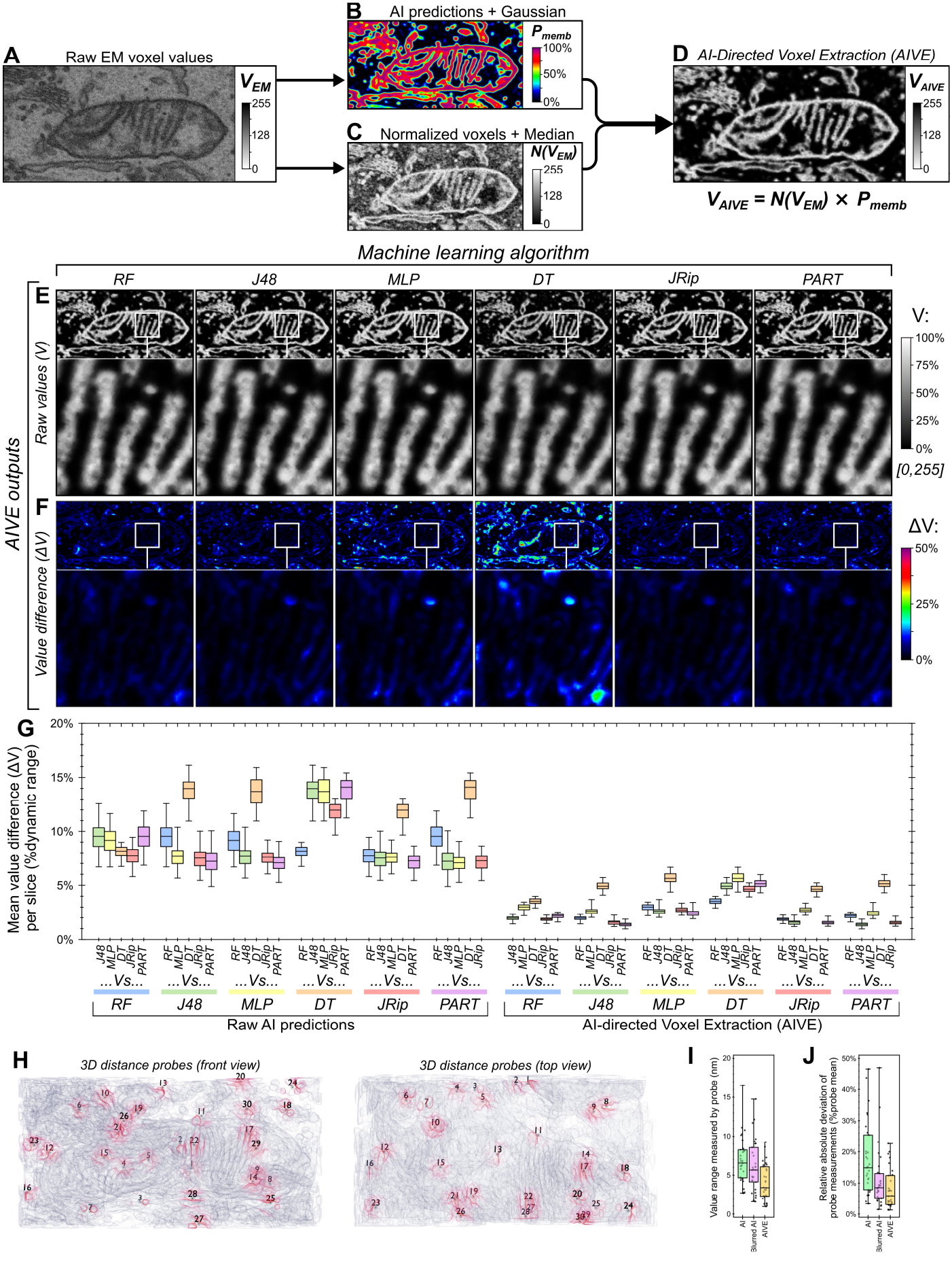
A
Raw EM voxel values
V_{EM}
255
128
0
B
AI predictions + Gaussian
P_{memb}
100%
50%
0%
C
Normalized voxels + Median
$N(V_{EM})$
255
128
0
D
AI-Directed Voxel Extraction (AIVE)
V_{AIVE}
255
128
0
$V_{AIVE} = N(V_{EM}) \times P_{memb}$
Machine learning algorithm
RF
J48
MLP
DT
JRip
PART
AIVE outputs
E
Raw values (V)
V:
100%
75%
50%
25%
0%
[0,255]
F
Value difference (ΔV)
ΔV:
50%
25%
0%
G
Mean value difference (ΔV) per slice (%dynamic range)
20%
15%
10%
5%
0%
...Vs...
Raw AI predictions
AI-directed Voxel Extraction (AIVE)
H
3D distance probes (front view)
3D distance probes (top view)
I
Value range measured by probe (nm)
AI
Blurred AI
AIVE
J
Relative absolute deviation of probe measurements (%probe mean)
50%
40%
30%
20%
10%
0%

Figure 3

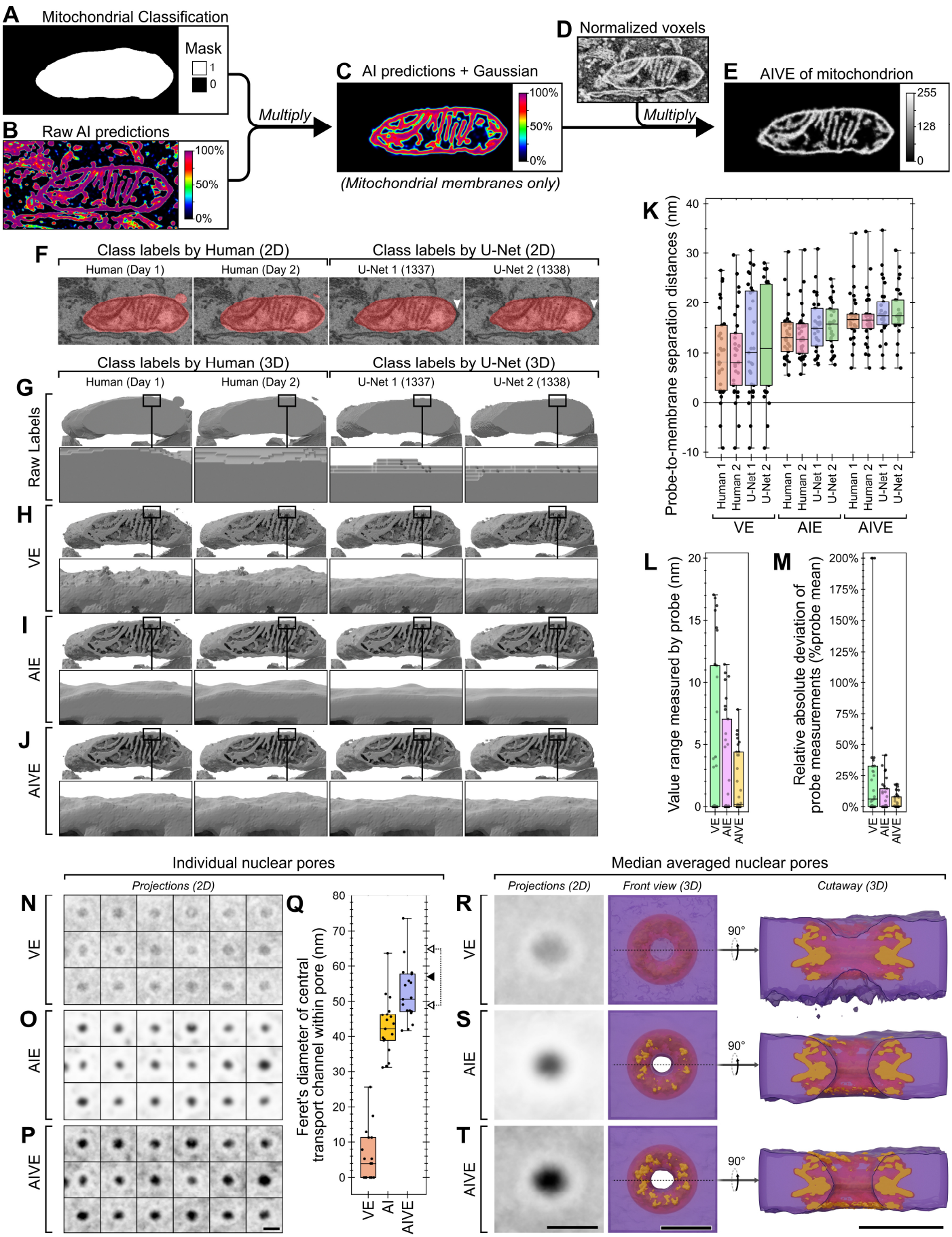
A Mitochondrial Classification
Mask
1
0
B Raw AI predictions
100%
50%
0%
Multiply
C AI predictions + Gaussian
100%
50%
0%
(Mitochondrial membranes only)
D Normalized voxels
Multiply
E AIVE of mitochondrion
255
128
0
F
Class labels by Human (2D)
Class labels by U-Net (2D)
Human (Day 1)
Human (Day 2)
U-Net 1 (1337)
U-Net 2 (1338)
G
Class labels by Human (3D)
Class labels by U-Net (3D)
Raw Labels
H
VE
I
AIE
J
AIVE
K
Probe-to-membrane separation distances (nm)
Human 1
Human 2
U-Net 1
U-Net 2
VE
AIE
AIVE
L
Value range measured by probe (nm)
M
Relative absolute deviation of probe measurements (%probe mean)
Individual nuclear pores
Projections (2D)
N
VE
O
AIE
P
AIVE
Q
Feret's diameter of central transport channel within pore (nm)
VE
AI
AIVE
Median averaged nuclear pores
Projections (2D)
Front view (3D)
Cutaway (3D)
R
VE
S
AIE
T
AIVE
90°

Figure 4

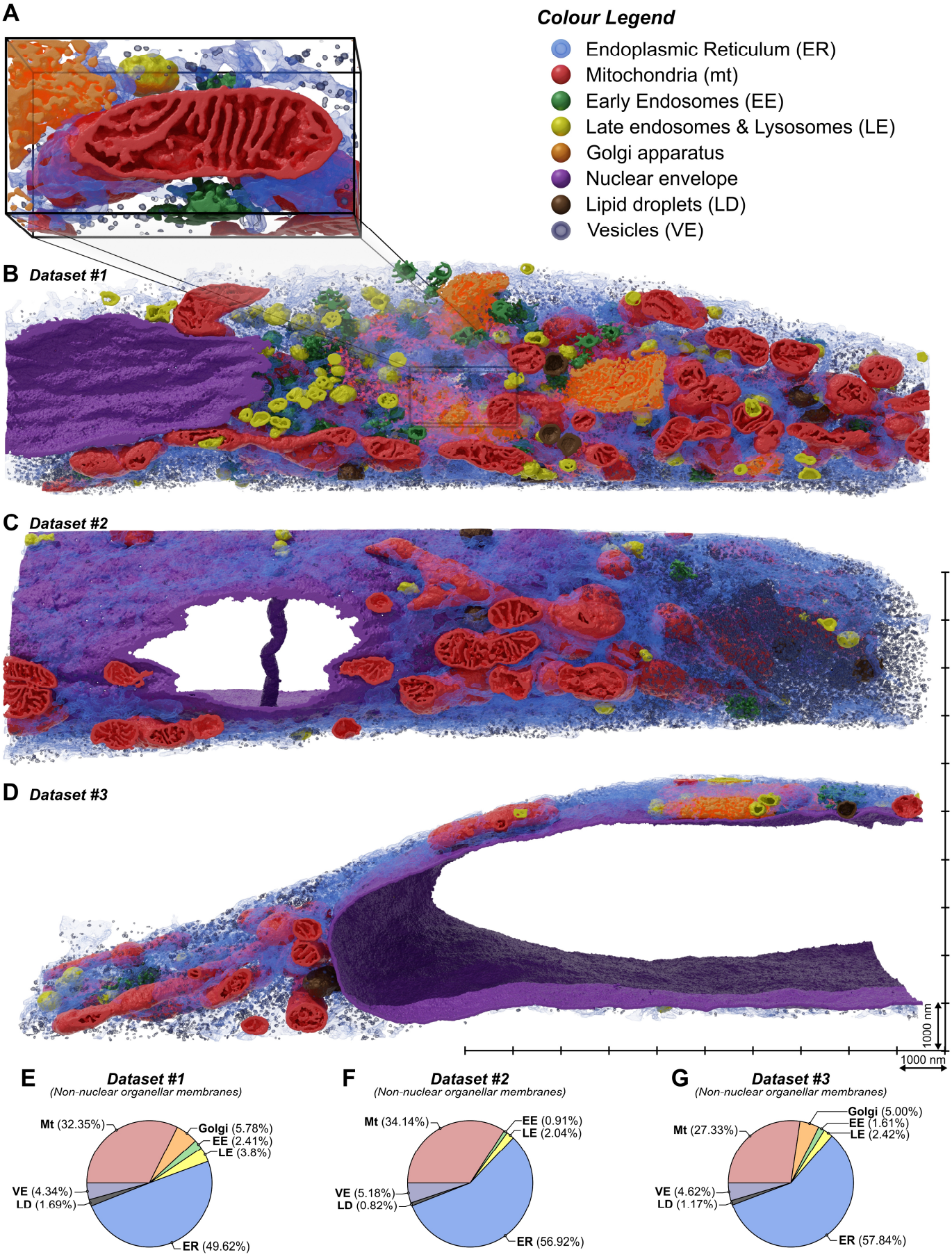
A
Colour Legend
Endoplasmic Reticulum (ER)
Mitochondria (mt)
Early Endosomes (EE)
Late endosomes & Lysosomes (LE)
Golgi apparatus
Nuclear envelope
Lipid droplets (LD)
Vesicles (VE)
B Dataset #1
C Dataset #2
D Dataset #3
1000 nm
1000 nm
E Dataset #1
(Non-nuclear organellar membranes)
Mt (32.35%)
Golgi (5.78%)
EE (2.41%)
LE (3.8%)
VE (4.34%)
LD (1.69%)
ER (49.62%)
F Dataset #2
(Non-nuclear organellar membranes)
Mt (34.14%)
EE (0.91%)
LE (2.04%)
VE (5.18%)
LD (0.82%)
ER (56.92%)
G Dataset #3
(Non-nuclear organellar membranes)
Golgi (5.00%)
EE (1.61%)
LE (2.42%)
Mt (27.33%)
VE (4.62%)
LD (1.17%)
ER (57.84%)

Figure 5

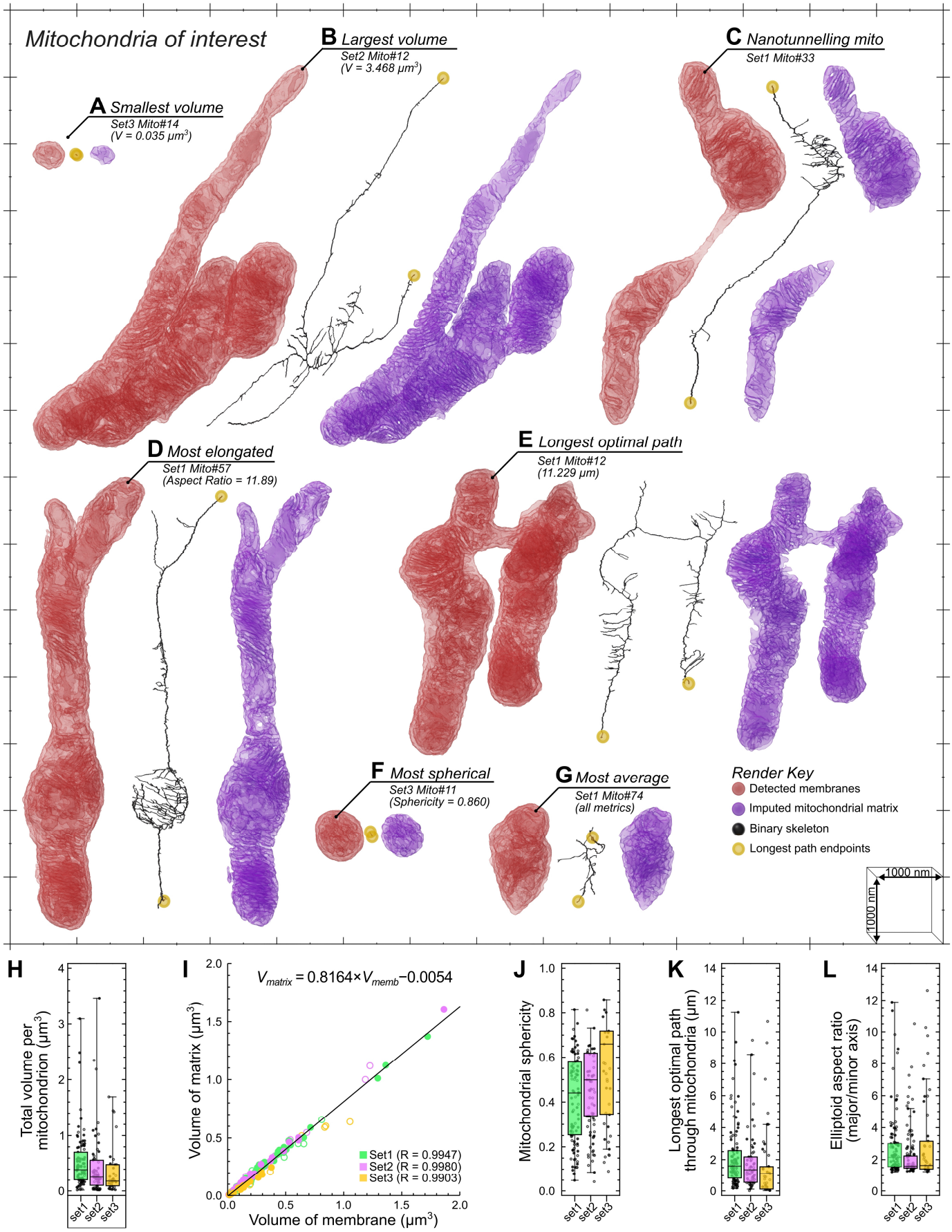
Mitochondria of interest
A Smallest volume
Set3 Mito#14
(V = 0.035 μm³)
B Largest volume
Set2 Mito#12
(V = 3.468 μm³)
C Nanotunnelling mito
Set1 Mito#33
D Most elongated
Set1 Mito#57
(Aspect Ratio = 11.89)
E Longest optimal path
Set1 Mito#12
(11.229 μm)
F Most spherical
Set3 Mito#11
(Sphericity = 0.860)
G Most average
Set1 Mito#74
(all metrics)
Render Key
Detected membranes
Imputed mitochondrial matrix
Binary skeleton
Longest path endpoints
1000 nm
1000 nm

H
Total volume per mitochondrion (μm³)
set1
set2
set3
I
$V_{matrix} = 0.8164 \times V_{memb} - 0.0054$
Volume of matrix (μm³)
Volume of membrane (μm³)
Set1 (R = 0.9947)
Set2 (R = 0.9980)
Set3 (R = 0.9903)
J
Mitochondrial sphericity
K
Longest optimal path through mitochondria (μm)
L
Ellipsoid aspect ratio (major/minor axis)

Figure 6

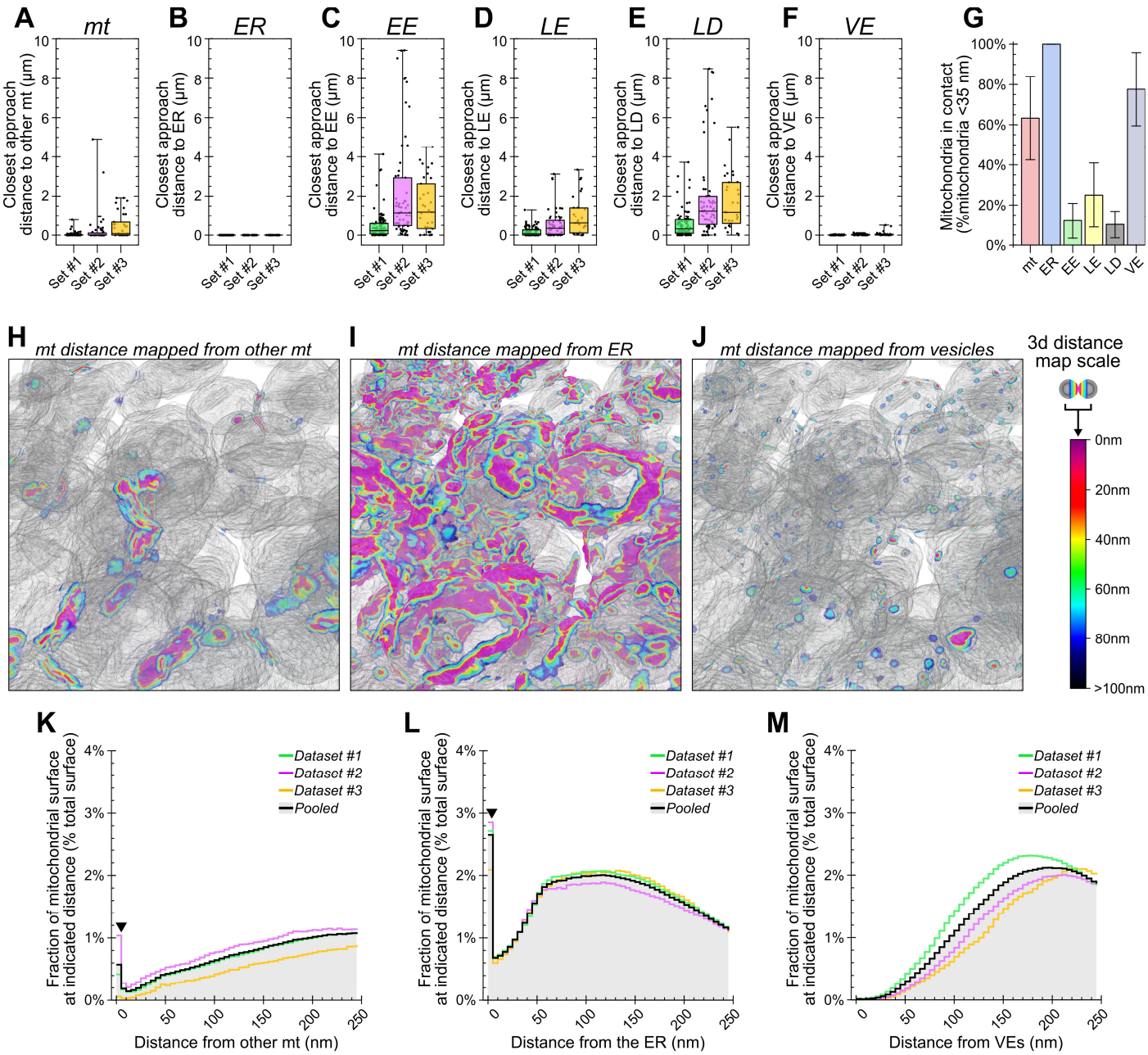
A
mt
Closest approach distance to other mt (µm)
B
ER
Closest approach distance to ER (µm)
C
EE
Closest approach distance to EE (µm)
D
LE
Closest approach distance to LE (µm)
E
LD
Closest approach distance to LD (µm)
F
VE
Closest approach distance to VE (µm)
Set #1
Set #2
Set #3
G
Mitochondria in contact (%mitochondria <35 nm)
mt
ER
EE
LE
LD
VE
H
mt distance mapped from other mt
I
mt distance mapped from ER
J
mt distance mapped from vesicles
3d distance map scale
0nm
20nm
40nm
60nm
80nm
>100nm
K
Fraction of mitochondrial surface at indicated distance (% total surface)
Dataset #1
Dataset #2
Dataset #3
Pooled
Distance from other mt (nm)
L
Distance from the ER (nm)
M
Distance from VEs (nm)

Figure 7

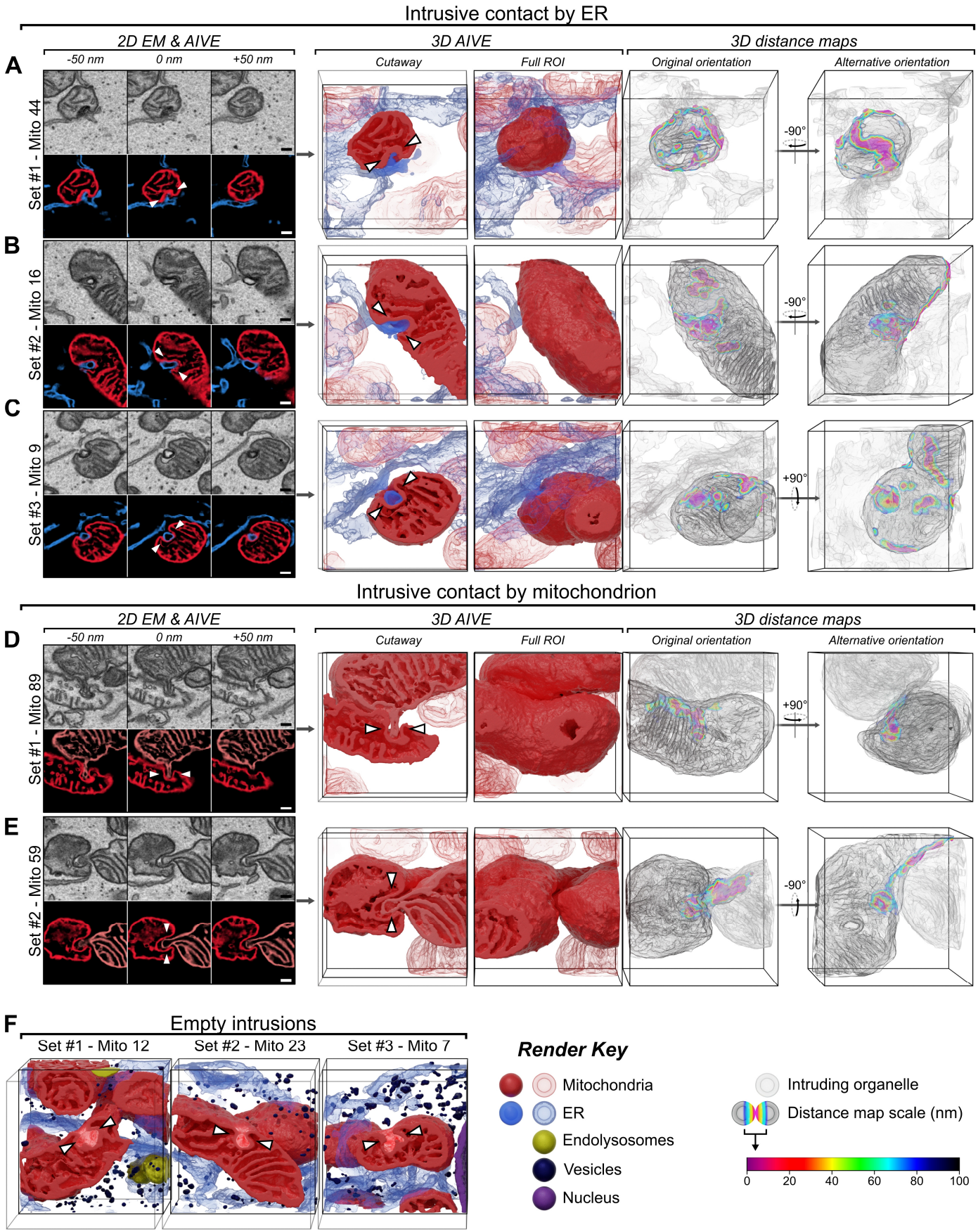
Intrusive contact by ER
2D EM & AIVE
3D AIVE
3D distance maps
-50 nm
0 nm
+50 nm
Cutaway
Full ROI
Original orientation
Alternative orientation
A
Set #1 - Mito 44
B
Set #2 - Mito 16
C
Set #3 - Mito 9
-90°
+90°
Intrusive contact by mitochondrion
D
Set #1 - Mito 89
E
Set #2 - Mito 59
F
Empty intrusions
Set #1 - Mito 12
Set #2 - Mito 23
Set #3 - Mito 7
Render Key
Mitochondria
ER
Endolysosomes
Vesicles
Nucleus
Intruding organelle
Distance map scale (nm)
0
20
40
60
80
100

Figure 8

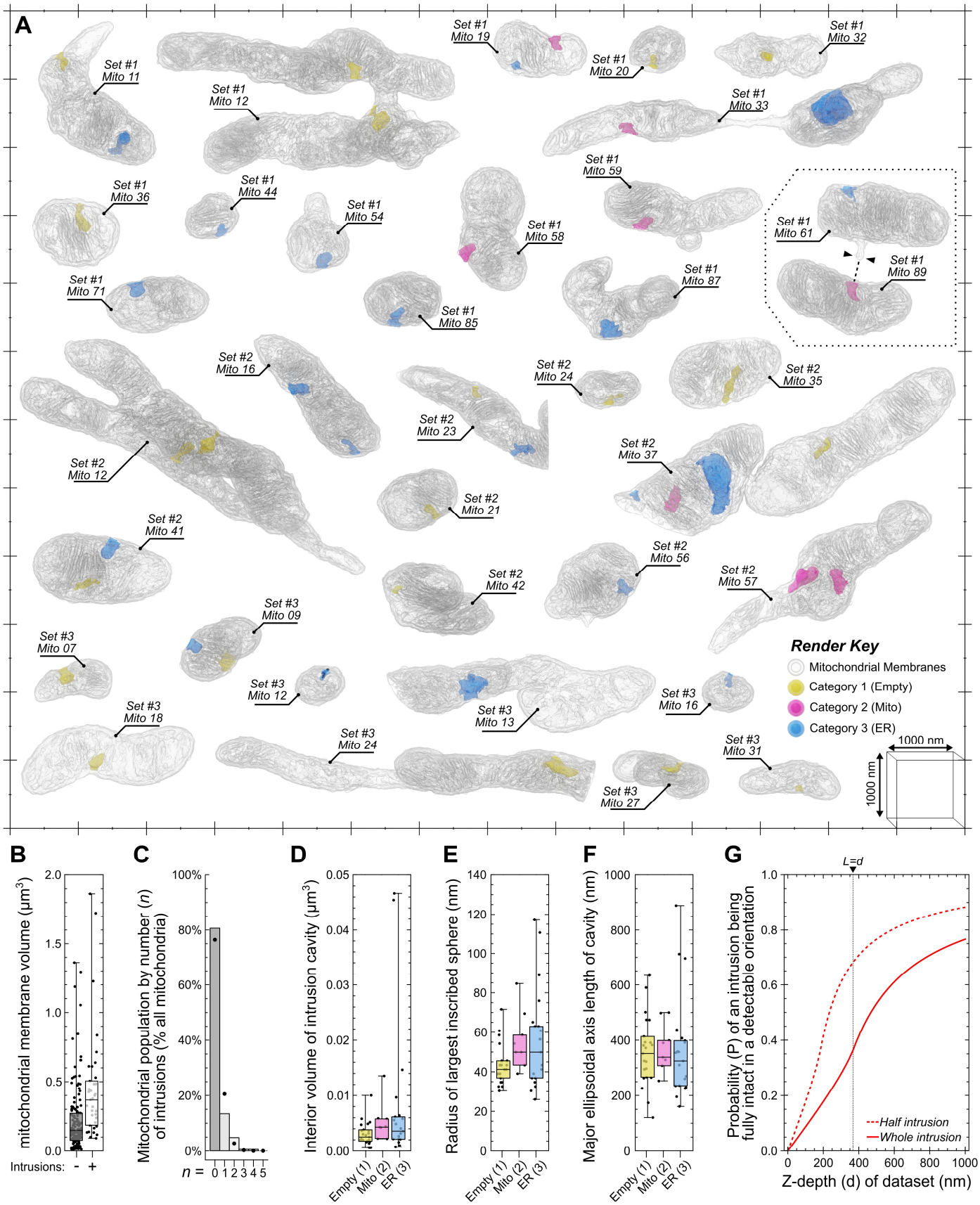
A
Set #1 Mito 11
Set #1 Mito 12
Set #1 Mito 19
Set #1 Mito 20
Set #1 Mito 32
Set #1 Mito 33
Set #1 Mito 36
Set #1 Mito 44
Set #1 Mito 54
Set #1 Mito 58
Set #1 Mito 59
Set #1 Mito 61
Set #1 Mito 89
Set #1 Mito 71
Set #1 Mito 85
Set #1 Mito 87
Set #2 Mito 16
Set #2 Mito 24
Set #2 Mito 35
Set #2 Mito 23
Set #2 Mito 12
Set #2 Mito 37
Set #2 Mito 21
Set #2 Mito 41
Set #2 Mito 56
Set #2 Mito 42
Set #2 Mito 57
Set #3 Mito 09
Set #3 Mito 07
Set #3 Mito 12
Set #3 Mito 16
Set #3 Mito 18
Set #3 Mito 13
Set #3 Mito 24
Set #3 Mito 31
Set #3 Mito 27
Render Key
Mitochondrial Membranes
Category 1 (Empty)
Category 2 (Mito)
Category 3 (ER)
1000 nm
1000 nm
B
mitochondrial membrane volume (µm³)
Intrusions: - +
C
Mitochondrial population by number (n) of intrusions (% all mitochondria)
n = 0 1 2 3 4 5
D
Interior volume of intrusion cavity (µm³)
Empty (1)
Mito (2)
ER (3)
E
Radius of largest inscribed sphere (nm)
Empty (1)
Mito (2)
ER (3)
F
Major ellipsoidal axis length of cavity (nm)
Empty (1)
Mito (2)
ER (3)
G
L=d
Probability (P) of an intrusion being fully intact in a detectable orientation
Half intrusion
Whole intrusion
Z-depth (d) of dataset (nm)